

Time-resolved rheometry of coarsening foams using three-dimensionally printed fractal vanes


Cite as: Phys. Fluids **34**, 113108 (2022); <https://doi.org/10.1063/5.0119944>

Submitted: 10 August 2022 • Accepted: 21 October 2022 • Published Online: 28 November 2022

 Igor M. Carraretto,  Crystal E. Owens and  Gareth H. McKinley

COLLECTIONS

Note: This paper is part of the special topic, Advanced Rheology of Complex Fluids for Next-Generation Technologies.

 This paper was selected as Featured



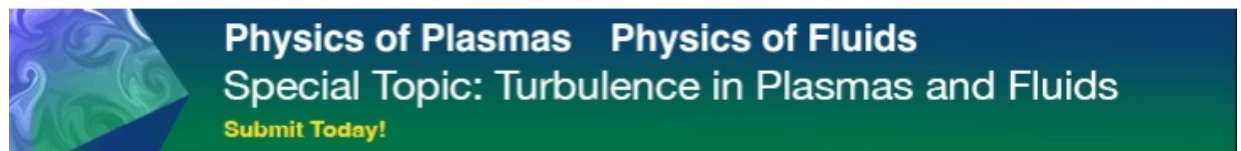
[View Online](#)



[Export Citation](#)



[CrossMark](#)



Physics of Plasmas Physics of Fluids
Special Topic: Turbulence in Plasmas and Fluids
Submit Today!

Time-resolved rheometry of coarsening foams using three-dimensionally printed fractal vanes

Cite as: Phys. Fluids **34**, 113108 (2022); doi: [10.1063/5.0119944](https://doi.org/10.1063/5.0119944)

Submitted: 10 August 2022 · Accepted: 21 October 2022 ·

Published Online: 28 November 2022



View Online



Export Citation



CrossMark

Igor M. Carraretto,^{1,2,a)}  Crystal E. Owens,¹  and Gareth H. McKinley¹ 

AFFILIATIONS

¹Hatsopoulos Microfluids Laboratory, Department of Mechanical Engineering, Massachusetts Institute of Technology, 77 Massachusetts Avenue, Cambridge, Massachusetts 02139, USA

²Dipartimento di Energia, Politecnico di Milano, via Lambruschini 4, 20156 Milano, Italy

Note: This paper is part of the special topic, Advanced Rheology of Complex Fluids for Next-Generation Technologies.

^{a)}Author to whom correspondence should be addressed: igormatteo.carraretto@polimi.it

ABSTRACT

Aqueous foams are useful in several applications, especially to reduce liquid loading in the oil and gas industry. The rheology of these foams evolves rapidly, and suitable constitutive models are required to describe the resulting multiphase flow. We describe a new experimental setup for advanced rheometry involving 4-arm and 12-arm vane-in-textured-cup toolsets. The cup was designed to provide *in situ* foaming to minimize injection times and flow-history artifacts before measurement, while the 12-arm vane was selected to eliminate slip and generate a homogeneous stress field in a weak foam. Using these tools, we measure the decay of linear viscoelasticity and yield stress and link the rheological evolution to optical measurements of the bubble size distribution. Time-resolved rheological measurements of the full flow curve of an aging foam are performed and used to construct a rheological master curve. Measurements of the transient linear viscoelastic response and observations of the bubble size distribution show that foams, after an initial induction period, experience an increase in the Sauter mean bubble radius that scales as $t^{1/2}$. Using the well-known Princen and Kiss model as a framework, we define a single unique time-dependent shift factor that varies with the Sauter mean bubble radius and enables us to use the rheological master curve to predict the temporal evolution of the foam's elastic and steady-state viscoplastic properties.

Published under an exclusive license by AIP Publishing. <https://doi.org/10.1063/5.0119944>

I. INTRODUCTION

Foams have numerous applications in food processing, cosmetics, textiles, metallurgy, and fire-fighting as well as flow assurance applications in the oil and gas industry (Schramm, 2006; Stevenson, 2012; Ellis and Lazidis, 2018). Specifically, within the oil and gas sector, foams have been employed in pipeline deliquification processes; foamed surfactants are introduced to reduce the residual liquid loading in horizontal pipelines that are used to transport untreated gas (Dall'Acqua *et al.*, 2017; Colombo *et al.*, 2018). In deliquification, foams are a promising alternative to traditional techniques that typically involve the use of cumbersome mechanical tools, such as compressors and “pigs,” which are mechanical devices that are inserted into a pipeline generally for the purpose of cleaning, gauging (indicating obstructions in the pipeline), or product separation (Tiratsoo, 2003). Due to the extensive use of foams in industrial applications, numerous studies on their rheology and flows have been published in the past two decades; see, for example, Briceno and Joseph (2003) in which the flow of uniform foam is considered as well as Bogdanovic *et al.* (2009) in which the flow of

various surfactant mixtures in stainless steel pipes (0.5 to 1 in. nominal diameter) has been analyzed. The latter work reports two different flow regimes: (1) the so-called “high-quality regime,” characterized by slug flow in which slugs (pockets) of gas are separated by walls or *septa* of intact foam, causing an oscillating pressure response upstream, and (2) the “low-quality regime” with uniformly distributed and homogeneous foam and a stabilized pressure response. Gajbhiye and Kam (2011) further investigated these distinct regimes, noting that the foam rheology in the high-quality regime depends on both the gas and liquid velocities, whereas in the low-quality regime only the gas velocity is influential. More recently, Parikh *et al.* (2019) have considered the process of foam generation and subsequent foam transport through pipelines as intrinsically coupled processes due to influences of the flow on the foam structure. However, in addition to empirical characterization of the different regimes in pipe flow, it is recognized that aqueous foams exhibit complex rheology (Polyanin *et al.*, 2002; Schramm, 2006), which must be understood to develop a predictive model of the material transport in pipes or other applications.

A. Rheological studies on foam

Aqueous foams are gas–liquid emulsions in which the gas bubbles are separated by thin liquid lamellae, yet the generated foam itself exhibits elastic solid-like behavior under small deformations, and as such, they combine mechanical characteristics of solids, liquids, and gases. At rest, foams exhibit a soft solid response with a small but finite shear stress that responds elastically to a small-imposed shear strain. However, as the strain increases, the foam deforms plastically due to local rearrangement of the bubbles that comprise the foam structure. If the applied stress is increased beyond the yield stress, the foam flows like a viscoplastic liquid as individual bubbles slide past one another. Eventually, at very high air volume fractions, foams can even become compressible (Saint-Jalmes *et al.*, 2012).

The first detailed rheological studies on aqueous foams and emulsions were published in the 1980s (Princen, 1983; 1985; Princen and Kiss, 1986; 1989; Khan and Armstrong, 1986; 1987), and expressions for key rheological properties, such as the yield stress and shear modulus of monodisperse foams and highly concentrated emulsions, were developed using a two-dimensional (2D) model of infinitely long cylindrical drops. The variables considered were the foam *quality* (or gas volume fraction, ϕ) of the dispersed phase, the bubble (or droplet) radius, the interfacial tension, Γ , the thickness of the thin liquid films separating adjacent drops, and the associated contact angle of the liquid films. One of the major outcomes was the independent correlation of the yield stress, σ_y , and the shear modulus, G , to the interfacial tension and the drop radius. Specifically, both are found to be proportional to the surface tension and inversely proportional to the drop radius (i.e., they depend on the Laplace pressure). For polydisperse foams (of most practical relevance for industrial applications), the relevant measure of the mean radius of the bubble size distribution is the Sauter mean radius $R_{32}(t)$, which is the ratio of the third moment of the radius distribution (\sim volume) to the second moment (\sim surface) (Stevenson, 2012).

In particular, Princen and Kiss (1989) determined the yield stress for a series of well-characterized, highly concentrated oil-in-water emulsions ($\phi > 0.74$). They employed a concentric-cylinder viscometer, in which a pool of mercury was placed in the center of the cup to eliminate end effects at the base of the cylindrical bob (Princen, 1986). The measurements were also corrected to account for slip (see, particularly, Princen and Kiss, 1989) because wall slip, if ignored, can lead to erroneous conclusions regarding the yield stress and the flow curve. For example, wall slip can be mistaken for hysteresis which is common in sheared foams (Princen and Kiss, 1989 and Subsection 1 of the Appendix). Wall slip may, in principle, be reduced or prevented by roughening of the walls. However, in the work of Princen and Kiss, the experiments were performed with smooth walls and then corrected by implementing the procedure reported in their paper; one may extract information on the “fluidity” of the slip layer from the pre-yield regime as it represents a pure slip with no shearing deformation. Although the observed linear slip behavior is purely empirical, it is unlikely to change as one passes through the yield stress of the bulk material; hence, assuming that the linear slip behavior continues beyond that point is reasonable, and through a simple subtraction, the effect of slip can be removed. After wall slip correction, the experimental results were well described by a viscoplastic model (known as the Bingham model) that can be written as

$$\sigma = \frac{\Gamma Y(\phi)\phi^{1/3}}{R_{32}} + C(\phi)\mu\left(\frac{\Gamma}{\mu R_{32}\dot{\gamma}}\right)^{1/2}\dot{\gamma}, \quad (1)$$

where the shear stress is σ , the yield stress is $\sigma_y = \Gamma Y(\phi)\phi^{1/3}/R_{32}$, and the capillary number is $Ca = R_{32}\mu\dot{\gamma}/\Gamma$. Here, Γ is the interfacial tension and μ is the viscosity of the liquid phase. The first term captures the solid-like yield stress present in the foam, and the second term describes the plastic flow beyond yield. The functions $Y(\phi)$ and $C(\phi)$ are experimentally determined and depend only on foam quality ϕ , $C(\phi)$ is order-unity while $Y(\phi)$ is typically 0.01–0.1 (Princen and Kiss, 1989; Herzhaft *et al.*, 2005).

Equation (1) can be nondimensionalized by the Laplace pressure, Γ/R_{32} , and written in the alternate form as follows:

$$\frac{\sigma}{\Gamma/R_{32}} = \frac{\sigma_y}{\Gamma/R_{32}} + C(\phi)Ca^{1/2}. \quad (2)$$

Hence, in steady shearing flow, emulsions and foams show a non-Newtonian behavior that is viscoplastic in character, and this feature has been reported in a wide number of studies (Höhler and Cohen-Addad, 2005).

One of the first pioneering studies on foam rheology and transport represented the flow of a liquid–gas foam by a modified Bingham plastic model (Calvert and Nezhati, 1986) with the addition of a liquid-rich slip layer caused by bubble migration away from a solid surface. The model was applied to experimental results for a cone-and-plate rheometer and also for pipe flow. It was found that the consistency [usually reported as K , which is a simple constant of proportionality, and in the case of a Newtonian fluid is equal to the viscosity μ (Pa s)] and the flow behavior (usually reported as n , which measures the degree to which the fluid is shear-thinning or shear-thickening) indices are, to a first approximation, independent of expansion ratio (ratio of the volume of a sample of foam to the volume of its base liquid) and bubble size, whereas the yield stress is dependent on bubble size distribution, and the slip layer thickness depends on the bubble size distribution and flow geometry. Herzhaft *et al.* (2005) studied the flow behavior of foams as a function of the gas volume fraction (ranging from 20% to 85%), at different static pressures and for various concentrations of added surfactant. The viscosity/shear stress curves of these foams again showed pronounced shear-thinning behavior beyond an apparent dynamic yield stress and approached an asymptotic power law form at high shear stresses, as consistent with Eq. (1). The authors noted that at a fixed high-volume fraction the shear viscosities obtained for various concentrations of added surfactant scale with the ratio of the interfacial tension to the Sauter mean diameter, reflecting the importance of the total interfacial area in the foam. Much additional work has been done, and two reviews have been published by Höhler and Cohen-Addad (2005) and Cohen-Addad and Höhler (2014), which report in rich detail the state of the art in the scientific understanding of foam and highly concentrated emulsions. Specifically, in the former review, the basic physics and physical chemistry of foams, experiments, numerical simulations, and theoretical models concerning foam rheology are reported, whereas the latter article reviews how the macroscopic mechanical response arises from a coupling between interfacial energy and long range molecular interactions, entropic effects, interfacial rheology, and dynamics at the droplet or bubble scale, reporting experiments and models on elasticity, osmotic pressure, yielding, and flow behavior. In

this review, they bridge the gap between generic models of the form of Eq. (1), currently proposed to explain the complex foam rheological behavior, and a fully theoretical approach that predicts quantitatively the constitutive response of foams from physicochemical properties of the constituents. Weaire (2008) has also broadly reviewed the rheology of foam, underlying the fact that liquid foam should be viewed as the appropriate prototype for the wide class of substances that exhibit both elasticity and a yield stress. Many additional rheological phenomena have been linked to small-scale deformations, slip, and shear banding inside foams. We highlight a few additional relevant studies here: Dinkgreve *et al.* (2016) have focused on different ways of measuring the yield stress, highlighting that creep experiments in foam can be difficult to interpret, because of the upturn in the creep compliance even for small stresses at long times, perhaps induced by changes in the microstructure of the unyielded foam. Ovarlez *et al.* (2013) describe the emergence of techniques that allow the measurement of local flow properties of a foam (i.e., the velocity and volume fraction fields) that have led to observation of new and complex behaviors. This potentially includes shear-banding in a homogeneous shear stress field, which cannot be accounted for by the standard steady-state constitutive laws of simple yield stress fluids and emphasizing that non-local constitutive models are needed to fully describe the flow of the foam. Most recently, Pitois and Rouyer (2019) studied the effect of solid particle addition on the rheological properties of a three-phase foam formulation. Depending on their hydrophobicity and size, the particles can adopt different geometrical configurations at the air-liquid interfaces, in the films, or in the interstices between the bubbles and can significantly modify the macroscopic rheological properties.

Ultimately, despite the various microstructural and kinematic complexities, the bulk macroscopic rheological response of each of these systems can all be written in the form of the familiar Herschel–Bulky equation as follows:

$$\sigma = \sigma_y(\phi) + K(\phi)\dot{\gamma}^n, \quad (3)$$

where $\sigma_y(\phi)$ is the yield stress and $K(\phi)$ is the consistency index of the foam; and as consistent with Eq. (1), we expect both the plastic and the viscous contributions to the stress to scale with the capillary pressure of the bubbles (based on the Sauter mean diameter), i.e., $\sigma \sim \Gamma/R_{32}$.

B. Time-resolved rheology of aging foam

In addition to this non-Newtonian behavior in steady flow, foams have an additional complexity: they are intrinsically unstable and tend to coarsen over time, meaning that there is gas diffusion from the smaller bubbles into the larger ones. In addition to foam coarsening, foams also evolve due to drainage as the liquid in between adjacent bubbles drains in response to gravity, and also due to coalescence, as neighboring bubbles combine when their shared liquid film ruptures. A detailed analysis of the physical mechanisms of coarsening goes beyond the scope of this paper, and the reader may refer to Gunton *et al.* (1983), Hilgenfeldt *et al.* (2001), Saint-Jalmes and Langevin (2002), and Saint-Jalmes (2006) for more details of the mechanisms involved. The net result of these mechanisms is that the transient rheological response of foams is multivariate, and the rheological response depends on both the evolving volume fraction $\phi(t)$ and the evolution in the bubble size distribution $R_{32}(t)$. To investigate this evolution, Durian *et al.* (1991) used the multiple light-scattering technique to

study the coarsening of a three-dimensional (3D) foam and reported that the average bubble diameter grows in time as t^z , where $z = 0.45 \pm 0.05$. Similar trends were confirmed in subsequent studies by Barik and Roy (2009) and Cantat *et al.* (2013). Specifically, the work of Barik and Roy (2009) studied the change in bubble size distribution in wet foam with ageing using microscope images, and they noted that the Sauter mean radius scales as $t^{1/3}$ at shorter timescale, whereas at longer time scales, a diffusive scaling behavior with $t^{1/2}$ is commonly used to describe the structural evolution of foam. Ultimately, the reader can refer to the book *Foam Structure and Dynamics* by Cantat *et al.* (2013) for an exhaustive and comprehensive description of the bubble radius evolution in time.

C. Context and scope of work

Over his career, Don Baird has exploited numerous advanced rheological techniques for next-generation technologies that have foundational connections to the work presented in this paper. Together with Collias (Collias *et al.*, 1994, Collias and Baird, 1995), he studied the rheology of microcellular foams to improve the mechanical properties of gas-filled polycarbonate composites. His group also promoted detailed studies of prolonged rheological transients to help understand the evolution of microstructure in multiphase complex fluids such as fiber-filled polymer melts (Lambert and Baird, 2017) and thermotropic liquid crystalline polymers (Qian and Baird, 2016); we use similar protocols in our work to study the transient evolution of aqueous foams. The present rheological study builds upon studies of the aging dynamics of Gillette foam by Durian *et al.* (1991) and Gopal and Durian (2003) and seeks to further our understanding of the evolving elastoviscoplastic rheology of transient aqueous foams, specifically the weak foams generated *in situ* and used for pipeline deliquification. Moreover, it aims to develop an understanding of how the evolution in the Sauter mean radius of the bubbles in the foam and measurements of the aging rheology of an aqueous foam are interconnected. To eliminate the effects of wall-slip in the foam as it coarsens and ages, we use textured rheometric tooling: specifically, a bespoke vane geometry and a grooved cylindrical cup. Two foams are studied: commercial Gillette Foamy Regular shaving cream ($\phi = 0.92$), which is often used as a readily reproducible benchmark multiphase yield stress fluid (Durian *et al.*, 1991; Gopal and Durian, 2003), and a commercial aqueous foam formulation used in pipeline transportation that is based on a Chimec surfactant (Colombo *et al.*, 2018). For both foams, oscillatory strain amplitude sweeps are first performed to identify the linear viscoelastic region and the transition to yielding. Subsequently, the rheological consequences of the aging processes in the two foams are studied at both constant and varying frequency. Finally, to understand foam stability and evolution with time for the weaker, more shear-sensitive Chimec foam (compared to the Gillette foam), repeated steady shear-rate sweeps are performed, and combined with independent optical measurements of the time-evolving bubble radius to correlate the transient evolution in the rheology and microstructure of the aging foam. A similar work was performed and published by Cohen-Addad *et al.* (1998), the authors investigated the coarsening process on the complex shear modulus of a three-dimensional aqueous foam. Specifically, it appeared evident that the viscoelastic response is governed by a broad spectrum of relaxation times and it was found that the complex shear moduli (measured as a function of frequency), at different foam ages, could be superposed on a single master curve using a scaling law.

TABLE I. Chimec surfactant composition (Colombo *et al.*, 2018).

Component	Concentration (wt. %)
Ammonium lauryl ether sulfate	5–10
Polyglycerol alkyl ethers	50–60
Propan-2-ol	10–20
2-Butoxyethan-1-ol	<5

II. MATERIALS AND METHODS

The rheological measurements were performed with a DHR-3 rheometer (Discovery Hybrid Rheometer 3, TA Instruments, New Castle, DE, USA) on two foams: commercial Gillette shaving cream (original formulation by Gillette Boston, MA, USA) and an aqueous surfactant foam [Chimec SpA, Pomezia (RM), Italy], which is currently used in pipeline deliquification procedures and whose composition is reported in Table I.

In both cases, a large-gap cylindrical cup-and-vane geometry set was used to perform the experiments; this configuration was selected due to the fragile mechanical nature of the foams and the large bubble sizes. Both cups were 3D printed, allowing us to form a grooved texture on the inner surface of the cylindrical sample container to minimize slip effects in the sample at the outer wall of the annular fluid

sample. To check for shear-induced structural changes in the foam, up/down stress sweeps were performed, and the grooved texture was found to substantially reduce the measured hysteresis in the flow curve (see Subsection 1 of the Appendix on the hysteresis analysis for a more comprehensive discussion). All experiments were performed at 25 °C with temperature controlled by a Peltier device (TA Instruments).

For the Gillette foam experiments, a standard 4-arm metal vane was selected [Figs. 1(a)–1(c)], and the foam was injected through an applicator nozzle directly into the textured cup to avoid large air pockets. Additional description of the tool and vane rheometry as well as the printable solid model file for the static cup used in the Gillette experiments are included in the supporting material of Owens *et al.* (2020). By contrast, for the weak aqueous Chimec foam (the reader might refer to Sec. III A), a 12-arm fractal vane was used [Figs. 2(a)–2(c)], resulting in more gentle handling of the foam, and a more homogeneous shear field than is provided by the 4-arm vane (Atkinson and Sherwood, 1992; Owens *et al.*, 2020; Chaparian *et al.*, 2022). For the shear-sensitive Chimec formulation, the foam was generated *in situ* according to the following procedure: (1) the necessary amounts of water and surfactant required to guarantee a surfactant concentration of 0.3 wt. % were placed in the cup above the aeration stone, which consisted of a stainless steel diffuser (2 μm pore size, OneBom) integrated into the rheometer cup [Fig. 2(d)]; (2) air flow was injected through a gas regulator (TA Instruments) at about 1 liter

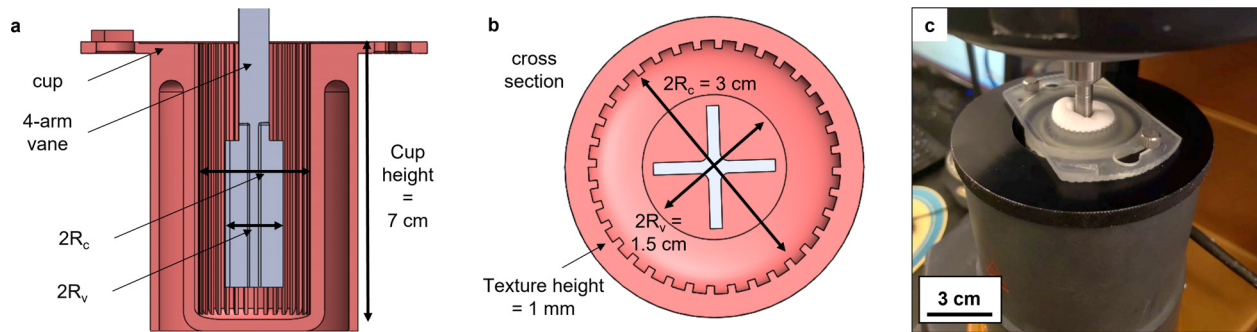


FIG. 1. (a) and (b) Schematic diagrams of the cup and 4-arm vane used for the experiments with Gillette foam; and (c) photograph of the cup and vane geometry and an aqueous liquid foam sample (in white) mounted inside the Couette fixture cooling jacket on the DHR-3 controlled-stress rheometer.

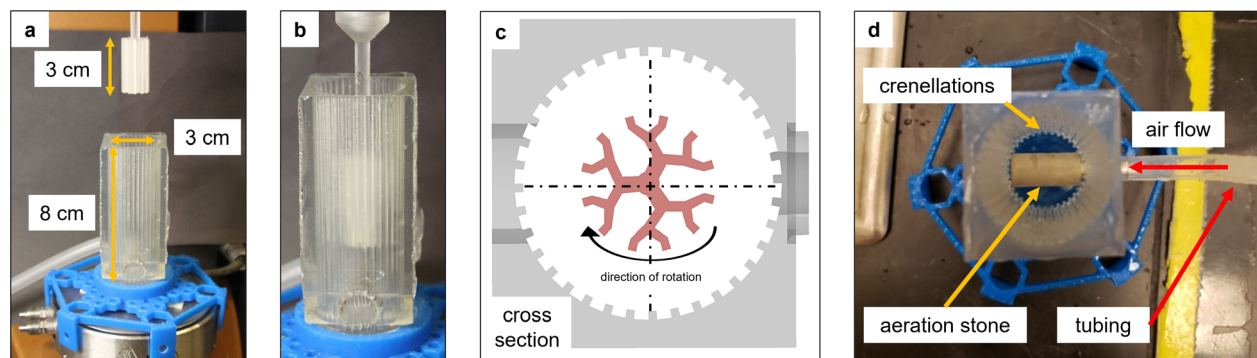


FIG. 2. (a) and (b) Side views; (c) cross section; and (d) top view of the 3D-printed cup used for *in situ* foam formation, showing the porous aeration stone mounted at the base of the crenellated cylindrical cup.

per minute, to generate *in situ* a foam with the required foam quality value, $0.85 \leq \phi \leq 0.99$ (depending on the test), on the rheometer itself directly before experiments. Additional design information regarding the foam-generating cup design and the 12-arm fractal vane used for the Chimec experiments is reported in Subsection 2 of the Appendix.

To analyze the resulting measurements (from either the 4-arm or 12-arm fractal vane) the following equation, developed in Owens *et al.* (2020) for a vane-in-cup geometry, was used to convert from measured torque [M (N m)] to shear stress [σ (Pa)] at the rim of the fixture:

$$M = 2\pi R_v^2 L \left[\left(1 - \frac{1.113}{N} \right) + \frac{R_v}{3L} \left(2.75 - \frac{3}{\sqrt{N}} \right) \right] \sigma, \quad (4)$$

where R_v is the vane radius in (m), L is the vane length in (m), and N is the number of vane arms. To evaluate the nominal shear rate in the foam at the edge of the fixture the following expression was used (Nguyen and Boger, 1987):

$$\dot{\gamma}(R_v) = \frac{2M}{dM/d\Omega}. \quad (5)$$

The reader is referred to Atkinson and Sherwood (1992) and Owens *et al.* (2020) for a more detailed description of the theoretical background for these expressions.

In tandem with rheometric measurements, another 3D printed device was constructed to image the process of foam creation and subsequent coarsening at high resolution. A stereolithographic 3D printed structure held an aeration stone below an enclosure with adjacent vertical parallel glass faces formed by two glass microscope slides separated by a narrow 1 mm gap. The foam that is formed at the bottom of the geometry is pushed upward between the glass plates as air is injected through the aeration stone. A time-lapse series of photographs of the microscopic evolution in 2D bubble shape against one glass face were taken every 100 s using a digital camera (Nikon D5100, 5× microscope objective), backlit through the narrow gap, at a height 22.5 mm above the aeration stone, corresponding to mid-height of the vane in a similar system. Pictures were analyzed with ImageJ (Java-based image processing program developed at the National Institutes of Health and freely available online) using a custom macro function to determine the bubble size distribution, the total number of bubbles $N(t)$, and the Sauter mean radius [$R_{32}(t)$] within each photograph.

III. RESULTS AND DISCUSSION

A. Linear viscoelasticity

To characterize the linear viscoelastic properties of the foams, strain amplitude sweeps were first performed both on fresh Gillette foam and on fresh Chimec foam as shown in Figs. 3(a) and 3(b), respectively, to determine the linear viscoelastic limit. In the case of the stiff Gillette foam, nonlinear deformation at $\omega = 10$ rad/s occurs at strains above $\gamma_0 = 10^{-2}$, whereas for the weaker Chimec foam, tests at two distinct frequencies ($\omega = 1, 10$ rad/s) show that nonlinear deformation only begins at higher strains above $\gamma_0 = 10^{-1}$. Below these limits, the storage modulus, G' , is approximately constant and much larger than the loss modulus, G'' , for both samples, as expected for soft solid-like elastic materials such as foams (Gopal and Durian, 2003). Beyond the critical strains, both foams begin to yield, and, at the largest strain amplitudes, the elastic modulus rapidly collapses and a liquid-like viscoplastic response is observed.

These aging aqueous foams show a strong time-dependent rheological behavior, as others have previously reported (Durian *et al.*, 1991). To better quantify this transient behavior, we performed two sets of experiments to monitor the time-varying evolution of the viscoelastic moduli. The first set of experiments consisted of a time sweep performed at a single constant frequency ($\omega = 10$ rad/s) to document the aging of the foam, and the second set employed repeated rapid frequency sweeps (from $\omega_i = 0.01$ rad/s to $\omega_f = 10$ rad/s) to explore the evolution in the frequency response of the material with sample age. The two protocols are both graphically indicated in Fig. 4(a). The results obtained for the Gillette foam using each protocol gave consistent results for G' and G'' at $\omega = 10$ rad/s, as shown in Figs. 4(b) and 4(c), confirming that the history of small-amplitude shearing in the two test protocols do not influence the aging of the foam. For both datasets, the timescale of material evolution, characterized by the mutation time, which is the characteristic time constant for the change in the material properties (Mours and Winter, 1994), was always much longer than the measurement time for each measured point (Subsection 3 of the Appendix), indicating that each data point represents the quasi-static rheological properties of the foam at that age time. A long induction time was observed for the Gillette foam shown in Fig. 4(c), indicating that the moduli remain relatively constant for the initial 10^3 s, after which the elastic modulus begins to decrease dramatically, as bubbles start coarsening. Meanwhile, the loss modulus measured at $\omega = 10$ rad/s initially decreases with time but then

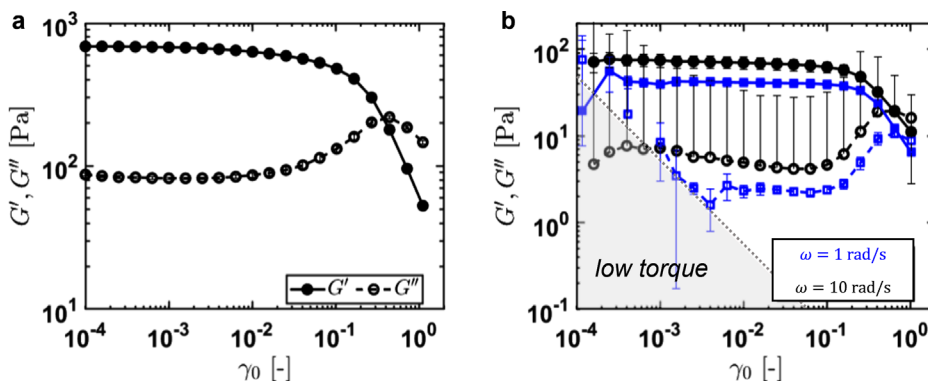


FIG. 3. Strain dependence of the viscoelastic properties for fresh foam samples: (a) a stiff Gillette foam ($\phi = 0.92$) measured using a 4-arm metal vane and 3D printed textured cup, $T = 25^\circ\text{C}$ and $\omega = 10$ rad/s, error bars are considerably smaller than the symbols themselves; hence, they cannot be seen (b) the much softer Chimec foam ($\phi = 0.97$) measured using a 12 arm 3D printed vane and 3D printed textured cup, $T = 25^\circ\text{C}$, $\omega = 10$ rad/s (black circles), and $\omega = 1$ rad/s (blue squares). The gray shaded region indicates the low torque limit of the transducer.

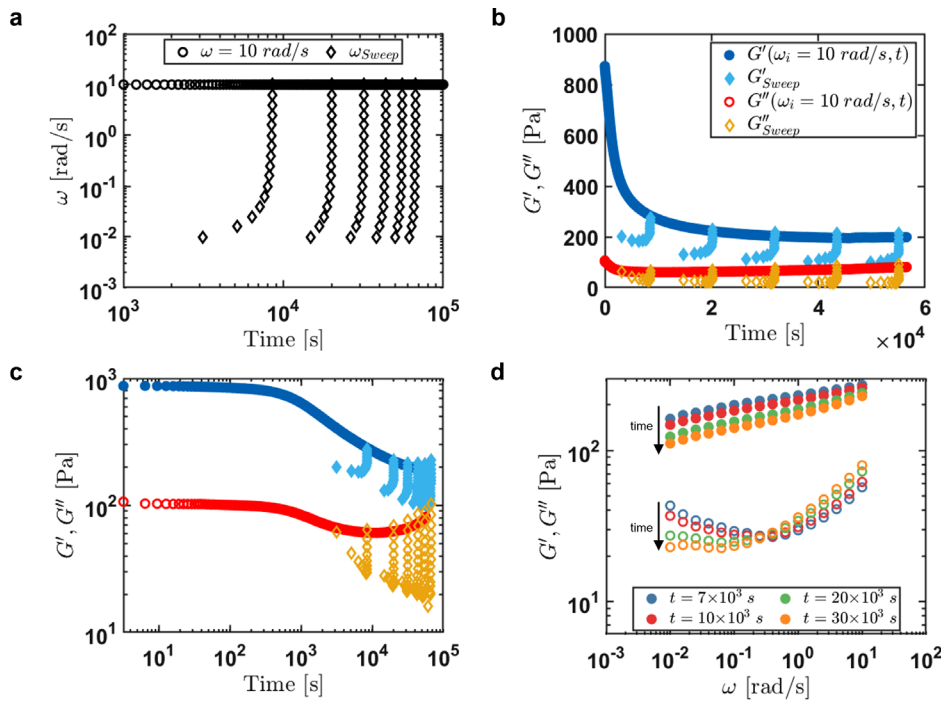


FIG. 4. Rheological aging of the elastic and viscous moduli (G' and G'') for Gillette foam using a 4-arm vane and a 3D printed textured cup at $T = 25^\circ\text{C}$ and $\gamma = 0.2\%$: (a) schematic of the two test protocols implemented; aging measurements were first taken at constant frequency $\omega = 10\text{ rad/s}$ (hollow circles) and then a repeated sequence of rapid frequency sweeps were performed on a fresh sample varying the frequency from $\omega = 0.01\text{ rad/s}$ to $\omega = 10\text{ rad/s}$ over a period of $66.8 \times 10^3\text{ s}$ (diamonds); (b) evolution of the storage and loss modulus reported on a linear scale, and (c) the same data reported on a logarithmic scale showing that the foam changes very little over the first 1000 s induction time and then begins to collapse and lose its viscoelasticity; and (d) evolution of the storage and loss moduli (G' and G'') as a function of angular frequency and time showing the power law dependence of the storage modulus (filled symbols) and the non-monotonic evolution of the loss modulus with time and frequency (hollow symbols). The arrow indicates how time increases.

increases again at very long times due to the increasing contribution of viscous effects in the collapsing foam at high frequencies. This non-monotonic behavior can be understood further by examining the frequency sweep results shown in Fig. 4(d). The frequency sweep measures each data point consecutively for each frequency and not simultaneously as shown in Fig. 4(a). However, because of the slow aging and low mutation number, we can compute the variations in G' and G'' with frequency at a single specific time point by curve-fitting the evolution in measured moduli as a function of time at specific frequencies and interpolating, with the single time point data reported in Fig. 4(d).

Specifically, starting from the experimentally determined values obtained through the frequency sweep, we split the variables: time and frequency. Initially, for each frequency both the values of the elastic and loss modulus were interpolated with a power law function of time, i.e., $G' = at^b$ and $G'' = ct^d$. Subsequently, four times were selected ($t = 7000, 10\,000, 20\,000, 30\,000\text{ s}$) and the values of elastic and loss modulus were retrieved for each frequency using the coefficients previously determined. The analysis was performed using a custom Matlab code. The elastic modulus $G'(\omega, t)$ increases with a power law behavior in frequency and decreases progressively with time for all measured frequencies. Meanwhile, in fresh foams G'' initially decreases with increasing frequencies, but above $\omega \approx 0.2\text{ rad/s}$, there is an upturn in the loss modulus indicating the increasing importance of viscous dissipation in the foam, especially at high frequencies. For this reason, the measured time-evolution of the loss modulus, G'' , shown in Fig. 4(c), first decreases, and subsequently increases again at long times, highlighting the importance of fully time-resolved frequency sweeps to tease out underlying material changes, perhaps associated with plasticity.

A similar test was conducted for the Chimec foam. However, due to the weaker, coarser, and faster-evolving foam structure, a 12-arm

fractal vane was used to produce a more homogeneous shear field than is possible with a 4-arm vane (Atkinson and Sherwood, 1992; Owens et al., 2020), and the frequency sweep was shortened to only span from 1 to 10 rad/s (corresponding to an experimental elapsed time of 50 s per sweep). Specifically, as reported in the work by Chaparian et al. (2022), the vane structure can have a strong impact on the fluid velocity field. There, two-dimensional Lagrangian simulations showed that few-arm ($N \leq 6$) cruciform vanes can significantly perturb the flow, adding a non-zero shear rate in the extensional direction and lobed yield surfaces. Meanwhile, many-arm ($N \geq 12$) fractal vanes, for which the vane's internal structural features are successfully "cloaked" by an almost cylindrical yield surface, lead to a more homogeneous deformation field in the sheared material and more reliable measurements of the shear stress compared to ground truth values. This computational measurement of the resulting computed torque on the fractal fixture using equations we have reproduced as Eqs. (4) and (5) showed much closer agreement with the baseline flow curve. We therefore selected a 12-arm vane to perform our *in situ* time-resolved rheological analysis on the weak foam. The results obtained both at a single frequency and with a repeated frequency sweep again agreed well as shown in Fig. 5(a). However, the Chimec foam is much weaker and has an induction time which is one order of magnitude shorter than for the Gillette sample, indicating that its foam structure deteriorates faster. When viewed on a logarithmic scale such as Fig. 5(b), small variations (in the range of $\pm 1\text{ Pa}$) can be seen in the values of the loss modulus (hollow diamonds) measured through repeated frequency sweeps and the values obtained through a time-resolved experiment at a single frequency (hollow red circles), this arises from the small differences in the deformation history experienced by the two different samples and provides a measure of the overall repeatability and magnitude of the experimental variability expected in our experimental measurements. Similar to our

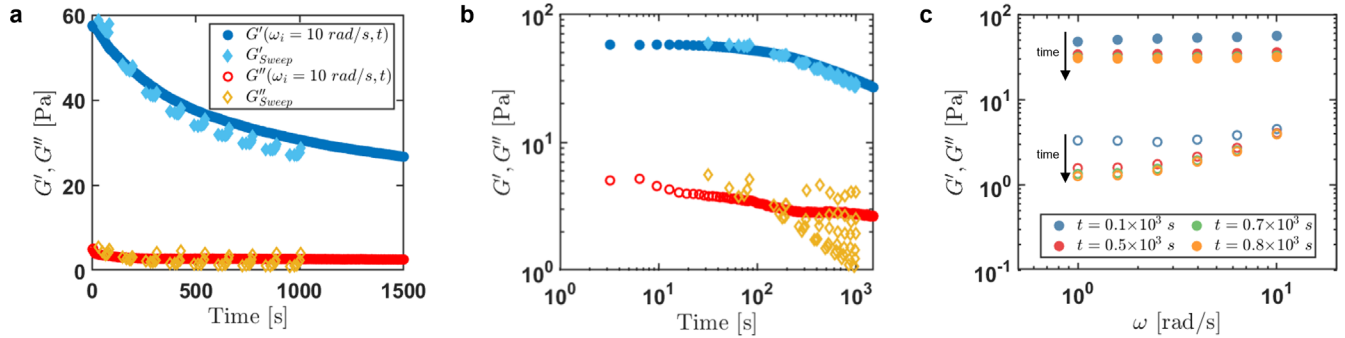


FIG. 5. Rheological aging of the elastic and viscous moduli (G' and G'') for Chimec foam ($\phi = 0.97$) using a 12-arm vane and a 3D printed cup at $T = 25^\circ\text{C}$ and $\gamma = 6\%$ at a constant $\omega = 10$ rad/s (circles) and then varying the frequency repeatedly (on a freshly generated sample) from 1 to 10 rad/s (diamonds): (a) evolution of the storage (filled) and loss (hollow) modulus reported on a linear scale, (b) data from (a) presented on a logarithmic scale to highlight the initial induction period, (c) evolution of G' and G'' as functions of angular frequency at different age times, for which the storage modulus is shown by the filled symbols and the loss modulus corresponds to hollow symbols). The arrow indicates how time increases.

experience with the Gillette foam, through the frequency sweep we were able to determine the variation in the elastic and viscous moduli (G' and G'') with both frequency and time [Fig. 5(c)] using the same procedure as before. The elastic modulus G' is nearly independent of frequency and slowly decreases as time increases, whereas the viscous modulus G'' increases with frequency (at a fixed time) and progressively reduces as time passes. Although all the values of $G''(\omega, t)$ decrease in magnitude with elapsed time, again the emergence of a more important viscous response is evident in Fig. 5(b) at higher frequencies ($\omega \sim 10$ rad/s) where the data remain nearly invariant over time.

B. Steady shear flow of aging foams

Measurements of the slowly evolving Gillette foam provide a good baseline for understanding foam evolution, while the more-rapidly mutating Chimec foam is particularly of interest as a commercial deliquifacant in pipe flow. We consequently performed steady shear rate tests with the Chimec foam, rotating the vane in a single direction in nonlinear deformations, to probe how the elastoviscoplastic properties in the foam evolve over time and how to model the influence of foam aging on the evolving shear rheology obtained for a set of constant shear rates.

As can be observed from Fig. 6(a), the steady shear flow curve was measured for the foam repeatedly as it evolved over 800 s (similar to the total time in Fig. 5). After this time, direct observation of the sample shows that the aging foam collapsed in height below the level of the top of the vane tool, rendering subsequent analysis of the measured torque inaccurate. For comparison, deliquification events in pipes are performed over seconds to minutes and thus correspond to relatively “young” foams (Carraretto et al., 2021). The evolution in the raw measured torque M and rotation rate Ω are reported in Fig. 6(a) as a function of time. A visual comparison suggests that the curves measured at each time are self-similar and, therefore, that a time-shear rate master curve can be constructed through the method of reduced variables with appropriate vertical and horizontal shifting.

Starting from Eq. (1), we see that if the bubble radius $R(t)$ increases with time due to coarsening, then we should expect both the yield stress [first term on the right-hand side of Eq. (1)] and the viscous term (second term on the right-hand side) to decrease with $R(t)$.

Hence, Eq. (1), which represents the rheological response of an ideal foam system, can be rewritten in general form as

$$\sigma(\dot{\gamma}, t) = \frac{\tilde{Y}(\phi)\Gamma}{R(t)} + C(\phi)\mu^n\Gamma^{1-n}R(t)^{n-1}\dot{\gamma}^n, \quad (6)$$

where $\tilde{Y}(\phi) = Y_0\phi^{1/3}$ and we have generalized the exponent for the viscous term to be represented by the parameter n , although it is found to be close to $n \approx 1/2$ in most foam systems.

Next, we define a vertical shift factor b_t to describe the time-dependent evolution of the stress and generate a reduced stress $\sigma_r = \sigma/b_t$. All terms in Eq. (6) are divided by b_t obtaining

$$\sigma_r = \frac{\sigma}{b_t} = \frac{\tilde{Y}(\phi)\Gamma}{b_t R(t)} + C(\phi)\mu^n\Gamma^{1-n}\frac{R(t)^{n-1}\dot{\gamma}^n}{b_t}. \quad (7)$$

This scaling factor b_t is expected to be a function of time and can, thus, be related to the evolution in radius $R(t)$ —or, more generally, for polydisperse systems to the Sauter mean radius $R_{32}(t)$ —and so we define the shifting parameter as $b_t \equiv R_{32}^0/R_{32}(t)$. Substituting this definition for b_t into Eq. (7), we obtain

$$\sigma_r = \frac{\tilde{Y}(\phi)\Gamma}{R_{32}^0} + C(\phi)\mu^n\Gamma^{1-n}(R_{32}^0)^{n-1}\left(\frac{\dot{\gamma}}{b_t}\right)^n. \quad (8)$$

This allows us to define a *reduced shear rate* $\dot{\gamma}_r = \dot{\gamma}/b_t$ in terms of the same shift factor. As a result, we expect that all of the time-resolved rheological data can be represented by a single constitutive expression or “master curve” that can be expressed in terms of the reduced variables $\{\dot{\gamma}_r, \sigma_r\}$ as follows:

$$\sigma_r = \frac{\tilde{Y}(\phi)\Gamma}{R_{32}^0} + C(\phi)\mu^n\Gamma^{1-n}(R_{32}^0)^{n-1}\dot{\gamma}_r^n, \quad (9a)$$

which can be written more clearly in simplified form as

$$\sigma_r = \sigma_y^{(0)} + K_0\dot{\gamma}_r^n. \quad (9b)$$

Here, $\sigma_y^{(0)}$ is the yield stress of the virgin foam (at time $t = 0$ s when the Sauter mean diameter is R_{32}^0 and the shift factor is $b_t = 1$), and K_0

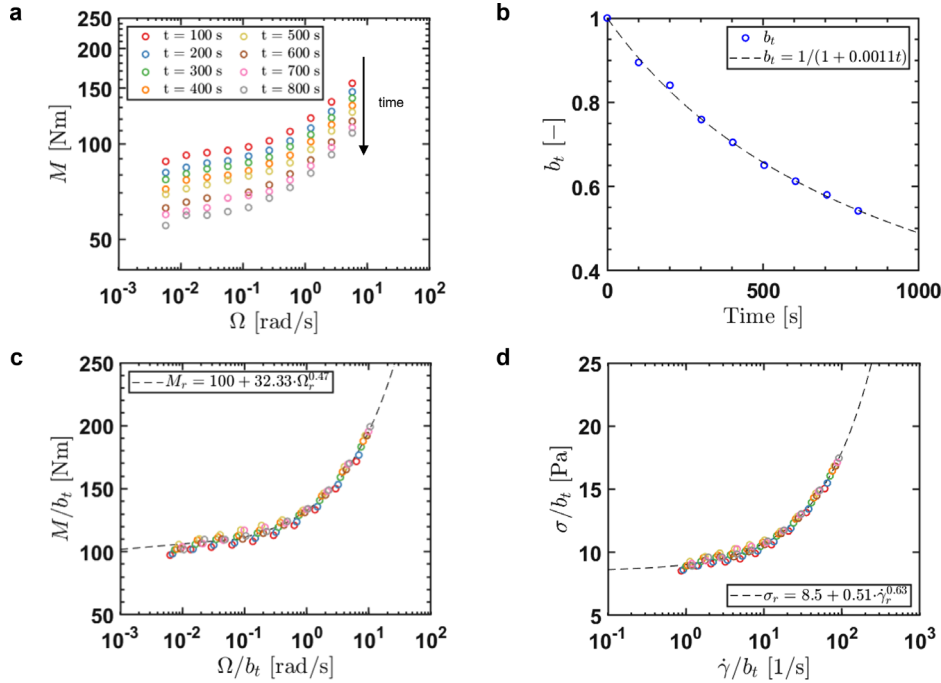


FIG. 6. Aging of the Chimec foam at a foam quality of $\phi = 0.97$. (a) Evolution with time of the measured torque vs rotational velocity for a fractal vane with $N=12$ arms in a 3D printed cup at $T=25^\circ\text{C}$. Time increases according to the arrow; (b) evolution in the vertical shift factor b_t as a function of time; (c) master curve constructed from the shifted torque and shifted rotational velocity using $t=0$ s as the reference age for the shift factor b_t ; and (d) time-age master curve in terms of the reduced shear stress and shear rate.

is a consistency index (depending on the viscosity of the fluid and the interfacial tension of the foam) which characterizes viscous dissipation in the sheared foam.

Based on the analysis above, it is clear that we should thus expect to be able to construct a rheological master curve by vertically shifting the stress and horizontally shifting the shear rate (or equivalently rearranging the measured torque and imposed rotational rate) using the same shift factor b_t for both variables. The time-dependent evolution in the resulting shift factor b_t [which is found manually by first vertically shifting the individual curves shown in Fig. 6(a)] is presented in Fig. 6(b). In this case, the shift factor b_t was found to be well-described by a simple hyperbolic fitting function that is empirically determined to be of the form

$$b_t = \frac{1}{1 + c_B t}, \quad (10)$$

where c_B is a fitting constant (found by regression to be $c_B = 0.0011 \text{ s}^{-1}$ for this foam quality, $\phi = 0.97$) and t is the elapsed time since the initial foam generation. The fitted values of b_t can then be used to construct the master curve in reduced raw variables as shown in Fig. 6(c), i.e., by plotting $M_0 = M/b_t$ vs $\Omega_0 = \Omega/b_t$. It is clear that this single time-dependent shift factor b_t produces a good data collapse for all of the flow curve measurements of the aging foam from $t = 0$ to 800 s.

As reported in the Introduction (Sec. 1A), the most successful constitutive equation to describe the rheological behavior of foam is the Herschel-Bulkley model [Eq. (3)], which allows us to relate the reduced raw variables through a functional relationship of the form

$$M_r = M_y^{(0)} + B_0 \Omega_r^\alpha. \quad (11)$$

With $M_y^{(0)} = 100 \pm 5 \mu\text{N m}$, $B_0 = 32.3 \frac{\mu\text{N m}}{(\text{rad/s})^\alpha}$, and $\alpha = 0.47$ with a root mean squared error (RMSE) of $2.75 \mu\text{N m}$ for the aging Chimec foam at a volume fraction of $\phi = 0.97$.

From these values, the measured torque can be converted to material stress using Eq. (4) and using the best fit relationship given in Eq. (11) the imposed angular rotation rate can be converted to a reduced material shear rate using Eq. (5). This results in the final rheological master curve shown in Fig. 6(d), again showing the same good level of superposition. Moreover, because of the nonlinear dependence between torque and rotation rate that is embodied in Eq. (11), computation of the shear rate from Eq. (5) results in a nonlinear mapping from the imposed rotation rate to computed shear rate, and this changes the power-law exponent of the best fits when expressed in either torque/rotation rate or shear stress/shear-rate coordinates.

Finally, to compare the measurements with a detailed, physically derived model such as Eq. (1) (Bingham equation), we now require a direct measure of the physical microstructure as it evolves during measurement, i.e., the foam bubble size distribution and the evolution of the Sauter mean radius $R_{32}(t)$, and to further compare that measurement with our expected value derived theoretically from the horizontal and vertical shift parameter $b_t \equiv R_{32}^0/R_{32}(t)$.

C. Evolution of bubble radius distribution with time

The rheological measurements and scaling arguments above indicate that there should be an inverse relationship between the yield stress in the foam and the Sauter mean diameter of the bubbles. The resulting master curve was expressed in terms of a dimensionless shift factor capturing the evolution in the mean bubble radius defined as

$$b_t \equiv \frac{R_{32}^0}{R_{32}(t)}. \quad (12)$$

This expression indicates that as the mean bubble radius increases with time and b_t decreases, the yield stress should decrease [as indeed observed in Fig. 6(a)]. The flow curves measured at each later time $t > 0$ s must,

thus, be shifted upwards (and to the right) to collapse onto the reference curve corresponding to $t=0$ s (when $b_i = 1$) (Dollet and Raufaste, 2014). To understand the expected functional form for $b(t)$, we directly analyzed the bubble radius evolution over time for the Chimec foam ($\phi = 0.97$) by visual observation according to the procedure reported in Materials and Methods. In Fig. 7, four photographs at the indicated times depict the evolution in bubble size and connectivity over time (Subsection 4 of the Appendix).

The Sauter mean radius was obtained by processing a series of similar photographs in ImageJ to identify the average radius of each imaged bubble, R_i , at each time point t_j , to calculate the bubble size distribution at each time. Specifically, the software ImageJ provided the perimeter of each bubble in pixels, assuming a circular bubble, the radius value was retrieved applying the simple geometrical formula of the disk (i.e., $R_i = \text{perimeter}/2\pi$), the obtained value was subsequently converted into millimeters. Each image typically captures $30 \leq N \leq 300$ bubbles per frame, and the ratio of the third moment to the second moment of the bubble size distribution then gives a value for $R_{32}(t_j)$:

$$R_{32}(t_j) = \frac{\sum_{i=1}^N R_i(t_j)^3}{\sum_{i=1}^N R_i(t_j)^2}. \quad (13)$$

As expected from typical coarsening behavior of foam, the Sauter mean radius (R_{32}) calculated using Eq. (13) increases monotonically with time (Fig. 8); meanwhile, the number of bubbles decreases within our view-frame and within the test sample. At very long times, the population becomes extremely polydisperse; however, at this point the foam has collapsed sufficiently that rheological measurements are no longer being made by the rheometer. The population information becomes noisier at long times due to fewer bubbles within the space accessible to imaging in our apparatus. In addition, the average

circularity for measured bubbles is around 0.59 with a standard deviation of 0.9, as evident from the images in Fig. 7 showing circular perimeters only at very short times. However, the radius values reported still provide a quantitative, if imperfect, measure of the time-varying evolution in the microstructure of the foam.

We seek to use this compact description of the bubble size distribution evolving in time to understand the evolution in the measurements of foam rheology. In Fig. 9(a), we plot the evolution of the mean bubble radius with time; although there are large fluctuations in the signal (for $t \geq 7500$ s) due to the relatively low total number of bubbles $\sum_i N_i$ in each image the results are consistent with the scaling $R_{32} \sim t^{1/2}$ expected from the work of Durian *et al.* (1991). In Fig. 9(b), we reproduce their measurements for the evolution of the mean bubble size in a Gillette foam that is the same composition as we studied rheologically in Fig. 4. When the data for each foam are represented on logarithmic-spaced axes, it is clear that there is an initial induction period when the mean bubble size is almost constant in time, and this is also consistent with the rheological measurements presented in Fig. 4(c). To quantitatively describe the evolution in measured bubble radius at both short and long times, we thus fit our measurements to an expression of the form:

$$R_{32}(t) = \left[(R_{32}^0)^2 + k_{32}t \right]^{1/2}, \quad (14)$$

which at long times predicts growth with $t^{1/2}$, but at short times predicts that the radius is nonzero and in fact is almost constant, as has been described before (Durian *et al.*, 1991). This model is consistent with our measured radius data in Fig. 9(b) within the measurement time window. The resulting parameter values for each foam are given in Table II. The larger initial radius and higher value of the rate constant for the Chimec foam reflects the weaker and more rapidly coarsening foam morphology. By balancing the relative magnitudes of the two terms on the right-hand side of Eq. (14), we can define a unique induction time in terms of these constants as

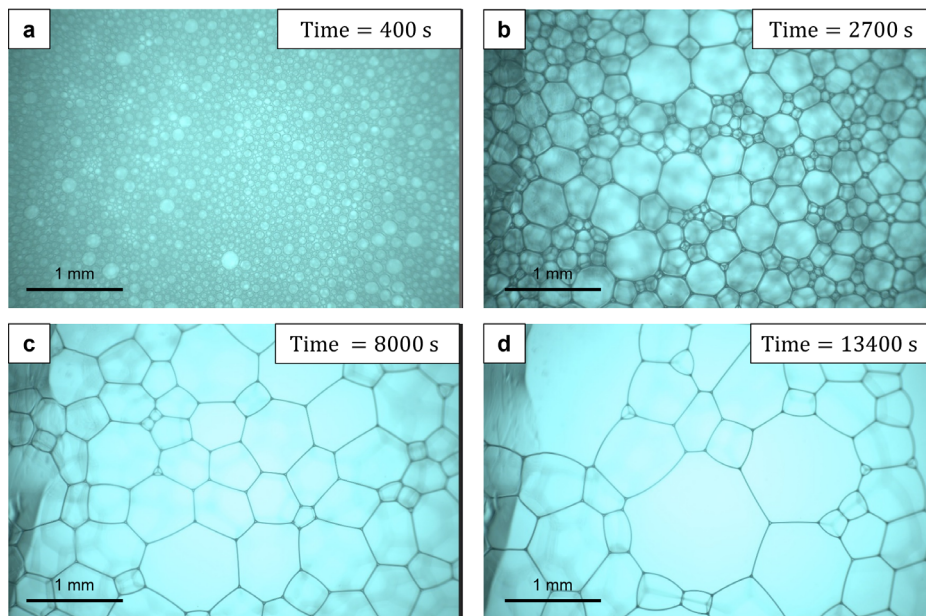


FIG. 7. Evolution of the Chimec foam microstructure at four points in time (initial foam quality $\phi = 0.97$): (a) time = 400 s; (b) time = 2700 s; (c) time = 8000 s; and (d) time = 13400 s.

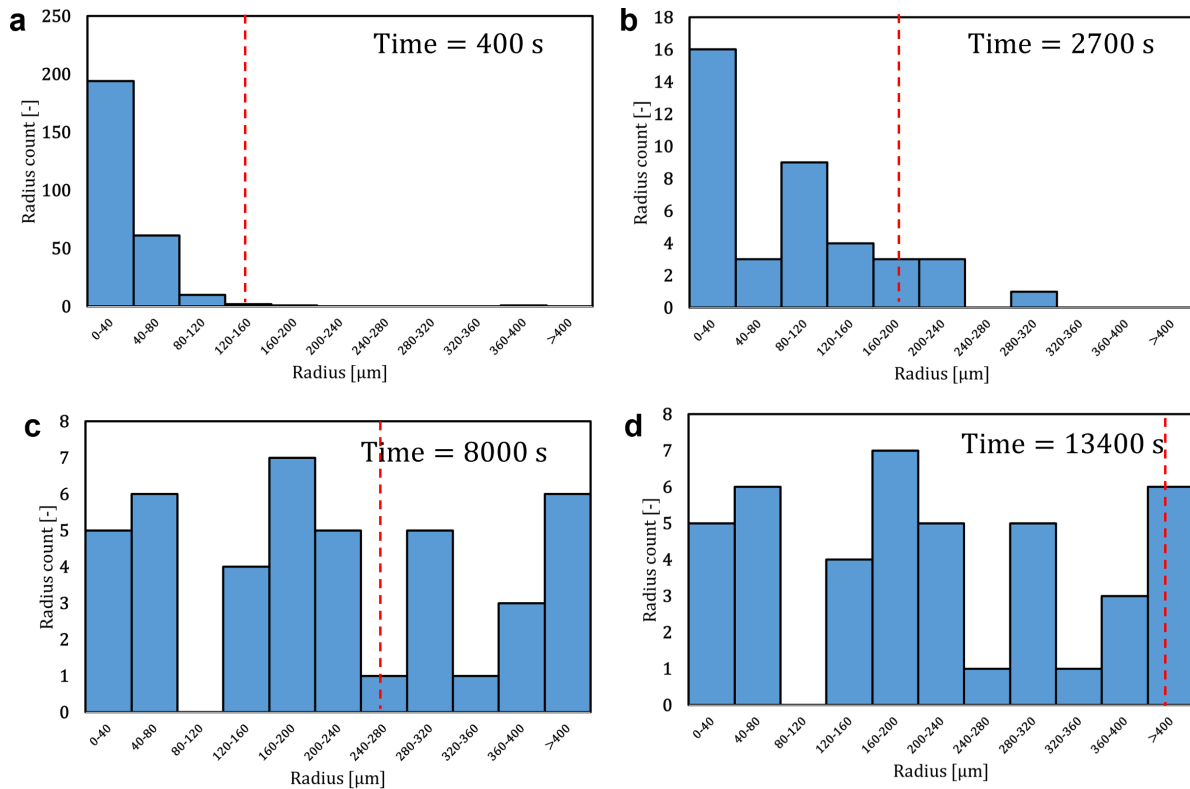


FIG. 8. Histograms showing the evolution of the bubble size distribution in the Chimec foam (initial $\phi = 0.97$). The dashed vertical red lines indicate the Sauter mean radius (a) $t_j = 400$ s, $R_{32} = 140$ μm , and $N = 269$, (b) $t_j = 2700$ s, $R_{32} = 190$ μm , and $N = 39$, (c) $t_j = 8000$ s, $R_{32} = 250$ μm , and $N = 43$, and (d) $t_j = 13400$ s, $R_{32} = 420$ μm and $N = 31$.

$$t_i = \frac{(R_{32}^0)^2}{k_{32}}, \quad (15)$$

which represents the characteristic timescale required by each foam to double its initial mean bubble radius, and this parameter allows us to discriminate between “short-time” and “long-time” regimes.

The corresponding values obtained for the two foams are different by a factor of five (Table II). This difference is similar to that already documented empirically through the measured induction times characterizing the decrease in linear viscoelasticity of the same foams (see Sec. III A) and is consistent with the considerably coarser initial structure of the Chimec foam.

Moreover, this effect might also arise in part due to different gas solubilities of each foam in the liquid phases. This has not been investigated in detail; however, in either case the net consequences are that the two foams behave qualitatively in similar fashion, but with a considerably different induction time.

At short times ($t \ll t_i$), a Taylor series expansion of Eq. (14) results in the expression

$$R_{32}(t) = R_{32}^0 \left[1 + \frac{k_{32}}{(R_{32}^0)^2} t \right]^{1/2} \approx R_{32}^0 + \frac{1}{2} \frac{k_{32}}{R_{32}^0} t + O(t^2) + \dots \quad (16)$$

Substituting this expression in our definition of the rheological shift factor in Eq. (12) results in an expression that is completely consistent with the functional form determined empirically. Comparing the measured evolution in mean bubble radius with the expected form for the shift factor b_t [Eqs. (10) and (12)], the aging constant c_B is found to be

$$c_B = \frac{k_{32}}{2(R_{32}^0)^2}. \quad (17)$$

In the original Princen and Kiss (1989) equation formulation, the yield stress is directly proportional to the surface tension (Γ), and inversely proportional to the mean radius of the microstructure. Incorporating our evolution equation for the mean bubble size, we thus estimate variations in yield stress to scale with the time-evolving Laplace pressure, as in Eq. (2) (which reports the relationship between yield stress, surface tension, and radius):

$$\sigma_y \sim \frac{\Gamma}{[(R_{32}^0)^2 + k_{32}t]^{1/2}}. \quad (18)$$

To generate additional insight on the influence of ϕ on the foam aging, the steady shear tests initially performed at a single foam quality of $\phi = 0.97$ were repeated for three more foam qualities: $\phi = 0.85$, 0.90 , and 0.99 , with five repetitions of each test. The resulting flow curves

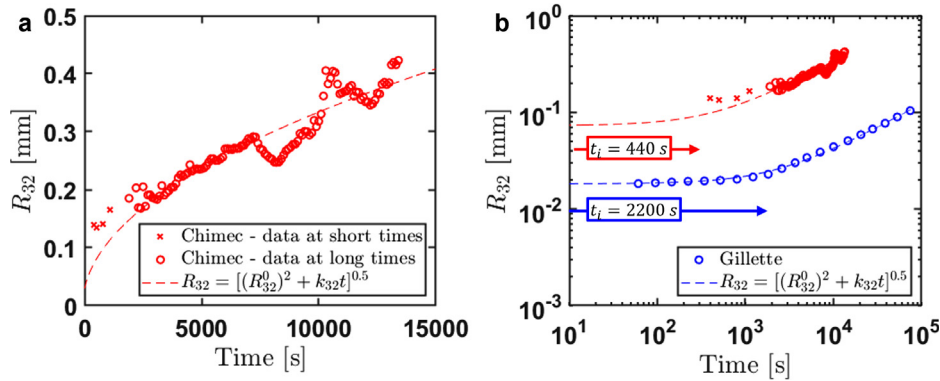


FIG. 9. (a) Evolution with time in the Sauter mean bubble radius for a Chimec foam ($\phi = 0.97$) and (b) the same data are represented on double logarithmic coordinates and compared with corresponding data for evolution in the mean bubble radius for a Gillette foam [data reproduced with permission from Durian *et al.*, Phys. Rev. A **44**, R7902 (1991)], for comparison.

TABLE II. Foam evolution parameters from Eq. (14).

Foam	R_{32}^0 (mm)	k_{32} (mm ² /s)	t_i (s)
Gillette	1.8×10^{-2}	1.47×10^{-7}	2200
Chimec	7.0×10^{-2}	1.11×10^{-5}	440

(converted from torque/rotation-rate to stress/shear-rate using the procedure outlined above) are reported in Figs. 10(a)–10(d), and each show qualitatively similar evolution of stress over time for each foam quality. In each case, rheology experiments were halted when the height of the aging foam fell below the top of the 12-arm vane. For more details on foam height decay rates and influence on the measured stress please refer to Subsection 5 of the Appendix. In all cases, a Herschel–Bulkley curve describes the measured data well, and the yield stress of the coarsening foams decreases over time. Each set of time-resolved flow curves can also be collapsed onto a master curve of the form given by Eq. (9) using a shift factor b_t [cf. Eq. (10)]. The three constitutive model parameters describing the flow curve for each composition are listed in Table III.

We find that c_B is approximately constant (within the experimental error range) for the foam qualities that we have studied, and no discernible trend with foam quality is apparent. This consistency in the value of the rate constant c_B shows that understanding the evolution in the yield stress for our foam with composition $\phi = 0.97$ is also sufficient for describing the temporal evolution of a suitably dimensionless yield stress for the range of tested foam qualities as shown in Fig. 11(a).

To completely describe the evolution of the material response in steady shear, both the yield stress and viscous contributions to the shear stress must be fully characterized, including their dependence on time and volume fraction. At high foam qualities we expect the yield stress to vary as

$$\sigma_y = \frac{\Gamma}{\left[(R_{32}^0)^2 + k_{32}t\right]^{1/2}} Y_0 \phi^{1/3}. \quad (19)$$

The dependence of the yield stress on volume fraction is very weak for the range of ϕ that are typically employed in foams as shown in Fig. 11(b). However, regression of the data for the initial material yield stresses (at $t = 0$ s) presented in Fig. 11(b) is broadly consistent with

this scaling and gives a best fit value of the single constant in the yield stress term as $Y_0 = 0.021 \pm 0.004$ and equivalently $\sigma_y^{(0)} = 8.00$ Pa. The resulting co-linear time-dependent evolution in both the measured yield stress and the average Laplace pressure [given by Eq. (19)] is illustrated by the parity plot presented in Fig. 12(a) for a foam quality of $\phi = 0.97$. We observe similar co-dependence for all of the weak aqueous Chimec foams regardless of foam quality (see Subsection 6 of the Appendix) and so we focus henceforth only on $\phi = 0.97$.

As we noted above in Sec. III B, the same time-dependent shift factor $b_t \equiv R_{32}^0/R_{32}(t)$ rescales both the plastic and viscous contributions to the stress in the aging foam [cf. Eqs. (7)–(9)]. Once the exponent, n , and the consistency K_0 are determined from regression to the master curve, the self-similar time-dependent evolution of the aging foam is then fully specified, in terms of the parameters given in Table III. The resulting time and rate-dependent rheological properties of the foam can then be expressed in the following form:

$$\sigma(\dot{\gamma}, t) = Y_0 \phi^{1/3} \frac{\Gamma}{R_{32}^0} \frac{R_{32}^0}{\left[(R_{32}^0)^2 + k_{32}t\right]^{1/2}} + K_0 \left[\frac{R_{32}^0}{\left[(R_{32}^0)^2 + k_{32}t\right]^{1/2}} \right]^{1-n} \dot{\gamma}^n. \quad (20)$$

The model predictions from Eq. (20) (dashed lines) are compared with the (unshifted) experimental data (dots) in Fig. 12(b), using $Y_0 = 0.021 \pm 0.004$. The predicted model curves agree well with the measurements in both the plastic and viscous-dominated regimes (i.e., at both low and high shear rates) for all measured times until the foam collapses (corresponding to $t \approx 800$ s) with errors of less than 1 Pa. The model reported in Eq. (20), in accordance with Princen and Kiss (1989), is valid for emulsions and foams with a quality $\phi \geq 0.74$, which is the case for all of the foams studied in the present work ($0.85 \leq \phi \leq 0.99$).

D. Connection to time-evolving linear viscoelasticity

Altogether, this analysis provides a rheological method for measuring and understanding the evolving constitutive response of transient sheared foams by relying on a microstructural description of the coarsening in the Sauter mean bubble radius of the foam. This presents a versatile approach for quantifying aging effects as it requires only

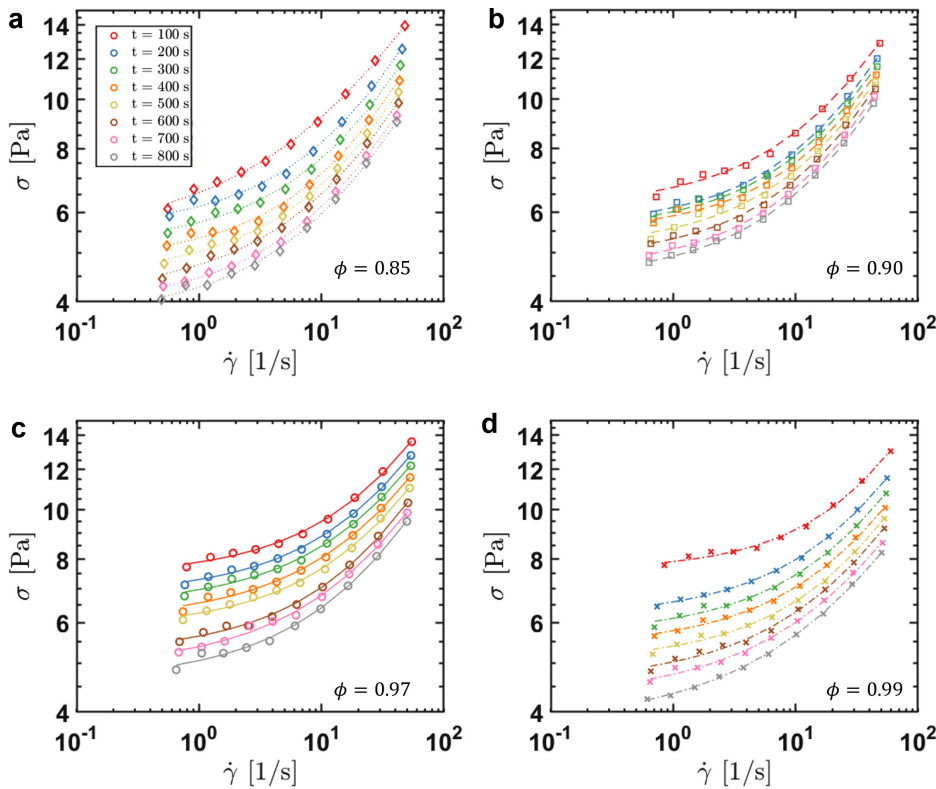


FIG. 10. Rheological aging in the measured flow curves for the Chimec aqueous foam at four different foam qualities measured with 12-arm fractal vane and 3D printed cup at $T = 25^\circ\text{C}$: (a) $\phi = 0.85$, (b) $\phi = 0.90$, (c) $\phi = 0.97$, and (d) $\phi = 0.99$. The data points shown for each curve are averaged over five sets of aging tests for each volume fraction ϕ using a newly generated foam for each set. Relative standard deviation between tests is below 10% for each ϕ . The corresponding collapsed master curves are shown in Subsection 6 of the Appendix.

TABLE III. Herschel–Bulkley parameters for a series of four different foam qualities, and the experimentally determined rate constant c_B describing the rate of aging in each foam. Errors in initial yield stress indicate $\pm 10\%$ for five repeated experiments.

ϕ (-)	$\sigma_y^{(0)}$ (Pa)	K_0 (Pa s ⁿ)	n (-)	c_B (s ⁻¹)
0.85	6.80 ± 0.68	0.74	0.61	0.001 14
0.90	6.60 ± 0.66	0.51	0.66	0.000 61
0.97	8.50 ± 0.85	0.51	0.63	0.001 10
0.99	8.00 ± 0.80	0.48	0.61	0.001 14

direct imaging or scattering data for the evolution in the mean foam radius, or conversely measurements of the time-evolving yield stress in steady shear, to understand most aspects of the nonlinear flow curve evolution through a single time-dependent shift factor b_t , or correspondingly the parameter c_B [see Eqs. (10) and (12)]. By linking the concept of a rheological master curve together with the scaling theory developed for emulsions and foams by Princen and Kiss, we can predict the evolving viscoplastic stress response of a foam over a range of material ages when it is subjected to a given shear rate and this provides useful input for simulating such aging of real foams during the pipeline deliquification process.

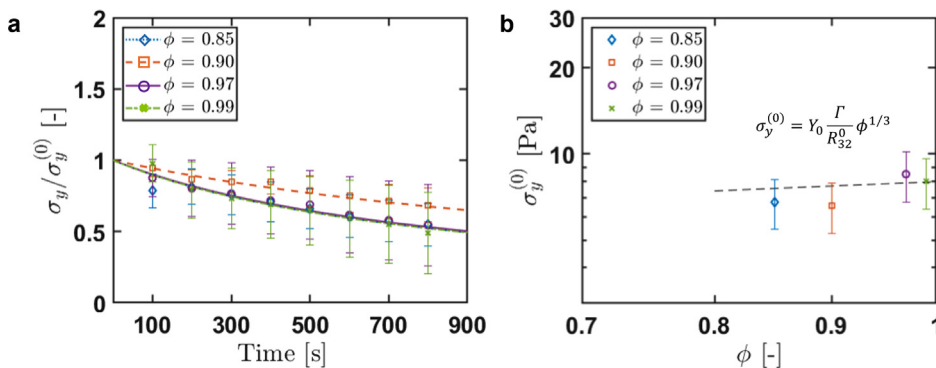


FIG. 11. (a) Yield stress evolution over time normalized by the initial value for the four different foam qualities of $\phi = 0.85$ (blue diamonds), $\phi = 0.90$ (orange squares), $\phi = 0.97$ (purple circles), and $\phi = 0.99$ (green crosses) and (b) variation in the initial yield stress as a function of foam quality, where the fitted model pre-factor for Eq. (19) (shown by the dashed line) is $Y_0 \Gamma / R_{32}^0 = 8.00$ Pa. Error bars indicate $\pm 10\%$ for five repeated experiments.

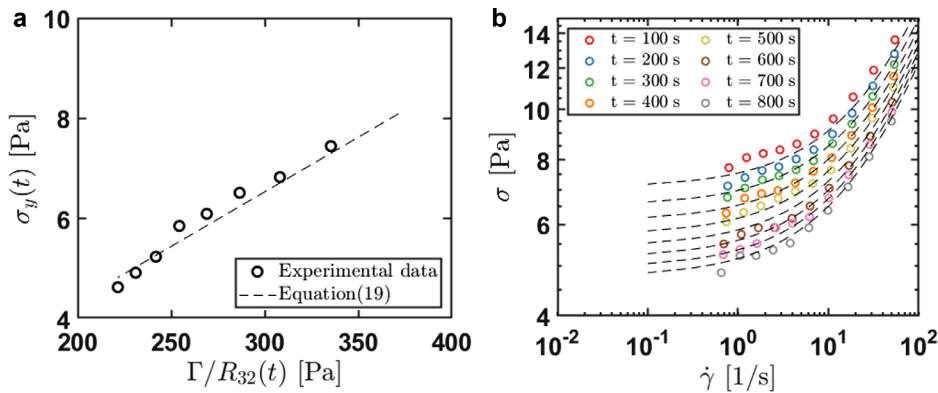


FIG. 12. (a) Correlation between the evolution in the measured yield stress and the average Laplace pressure in the bubbles (based on the Sauter mean radius computed from data such as that shown in Figs. 7 and 8) for the Chimec foam (foam quality $\phi = 0.97$) and (b) measured flow curves of shear stress vs shear rate with the overlaid model given by Eq. (20).

Finally, to complete our understanding, we compare the variation of the empirically derived shift factor, b_t , determined from steady-shearing measurements with our observations of the time-evolving linear viscoelastic properties of the $\phi = 0.97$ foam. In Fig. 13(a), we show the evolution in b_t determined from measurements of the steady shear rheology (symbols) compared directly with the expected relationship determined from imaging of the coarsening dynamics, $[R_{32}^0/R_{32}(t)]$, given by Eq. (14). This additionally confirms that the Laplace pressure is the relevant scale for the evolution of the shear stress.

In Fig. 13(b), we also compare the same evolution in $R_{32}^0/R_{32}(t)$ with the measured time-dependent change in the elastic modulus of the foam, measured in Sec. III A. It is clear that the age-dependent decrease in the elastic modulus of the foam correlates well with the progressive coarsening in the mean bubble size of the foam, additionally confirming that the radius evolution, and thereby the Laplace pressure, is the relevant underlying parameter for the evolution of the linear elastic modulus for our foam. Additional information on shifting of the elastic and viscous moduli for the Chimec and Gillette foam using the same evolution in Sauter mean radius are reported in Subsection 7 of the Appendix. In Fig. 13(c), the elastic modulus is plotted as a function of the inverse of the bubble radius, showing a consistent trend to what was expected. Laboratory studies of pipeline

deliquification (Carraretto *et al.*, 2021) show that these weak aqueous foams tend to coarsen and decay as they are advected along the pipe, and so an appropriate constitutive model must take into account the rheological variations in both time and axial position to generate an accurate flow simulation. Specifically, in industrial applications this understanding can help identify the number of surfactants injection points as the foam coarsens and the yield stress decreases, which leads to a progressive loss in its liquid removal efficiency. The results such as Eq. (19) for the yield stress and Eq. (20) for the full viscoplastic constitutive behavior allow dynamical simulations based on initial foam quality, surface tension, and material age; hence, the rheological properties of the foam can be optimized *ex situ* through such a computational analysis in combination with process requirements such as flow rates, number of allowable injection points, amount of water to be removed, and cost limits of the surfactant.

IV. CONCLUSIONS

In this work, we have studied the time-evolving elastoviscoplastic rheology of transient aqueous foams motivated by applications in pipeline deliquification. To measure the key rheological features of this transient foam as it evolves in time under the application of an external shear stress, we used a new experimental configuration to generate foam *in situ* and thereby perform accurate rheometry on undisturbed,

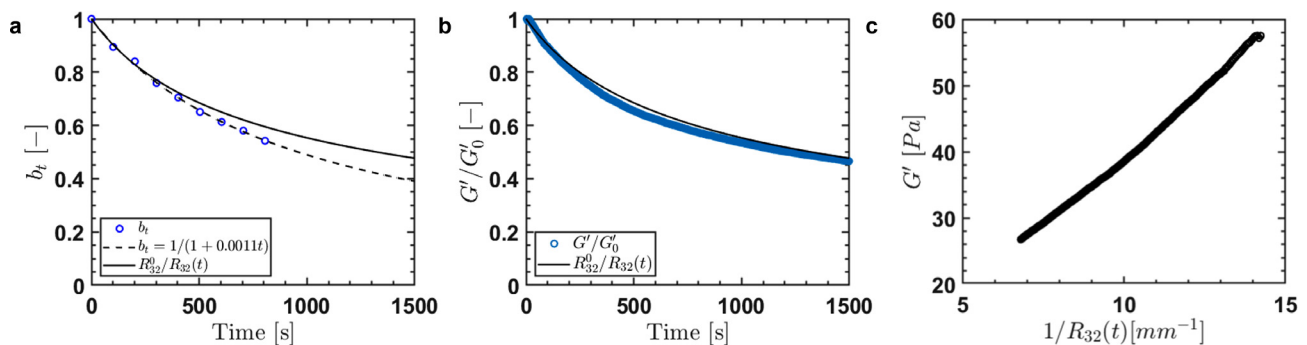


FIG. 13. (a) Evolution in the empirically determined vertical shift factor b_t and the Sauter mean radius evolution vs time for the $\phi = 0.97$ foam; (b) comparison of the evolution in the elastic modulus $G'(\omega, t)/G'_0$ (reported at $\omega = 1\text{ rad/s}$) and the Sauter mean radius evolution vs time; and (c) evolution of the elastic modulus $G'(\omega, t)$ as function of the inverse of radius.

low liquid-phase volume foams (gas fraction $85 \leq \phi \leq 99$ vol. %). Linear viscoelastic measurements using a fractal vane configuration show that, after an induction period (i.e., an initial time period over which the gas bubbles do not coarsen appreciably) of $t_i \approx 440$ s for the Chimec foam and ≈ 2200 s for the Gillette foam, both the elastic modulus and the yield stress decrease steadily with time due to bubble coarsening. Direct imaging of the evolving bubble radius distribution show that this elastoplastic aging can be well described in terms of a single dimensionless shift factor b_t [Eq. (12)], which can be compactly expressed in the form of Eq. (14) and which predicts that the increase in the Sauter mean radius scales as $t^{1/2}$, at long times, in accordance with previous measurements. Rheological measurements of the evolution in the full viscoplastic flow curve of the aging foams can be described with good accuracy by the well-known Princen and Kiss model, in conjunction with this same shift factor, which enables the time-resolved data to be collapsed onto a single shear-rate–age master curve for each foam composition. In this work, time-resolved rheological measurements of the full flow curve of a weak aging foam have been performed, laying the foundation for understanding and modeling the transient dynamics of foams in industrial applications. Specifically, the viscoplastic master curve represents the time-resolved rheological data in a simple way that can readily be incorporated into simulations of complex three-phase flows to predict how a transient foam will deform and evolve within complex flow geometries, enabling more reliable process control and design of more economical foam compositions.

ACKNOWLEDGMENTS

I.M.C. was supported by both the Italian Ministry of University and Research (MUR) through the Italian Ph.D. Scholarship, and by the Progetto Roberto Rocca through the Rocca Fellowship. C.E.O. was supported by the United States Department of Defense (DoD) through the National Defense Science and Engineering Graduate Fellowship (NDSEG) Program and through a MathWorks Engineering Fellowship. The authors thank Professor Douglas J. Durian for helpful discussion and Dr. Agnese Graziosi for helpful support with analysis of bubble photographs in ImageJ.

AUTHOR DECLARATIONS

Conflict of Interest

The authors have no conflicts to disclose.

Author Contributions

Igor Matteo Carraretto: Conceptualization (lead); Data curation (equal); Formal analysis (equal); Funding acquisition (lead); Methodology (equal); Writing – original draft (equal). **Crystal Elaine Owens:** Investigation (equal); Methodology (equal); Software (lead); Supervision (supporting); Writing – original draft (equal); Writing – review & editing (equal). **Gareth H. McKinley:** Conceptualization (supporting); Resources (lead); Writing – review & editing (lead).

DATA AVAILABILITY

The data that support the findings of this study are available from the corresponding author upon reasonable request.

APPENDIX: SUPPORTING INFORMATION

1. Hysteresis of foams

Foams belong to the class of soft glassy materials that broadly includes colloidal gels, clay suspensions, emulsions, and more. These materials display a challenging set of behaviors as the applied strain (or stress) often disrupts and rearranges the microstructure both in space and time leading to heterogeneous and time-dependent flow properties (Ovarlez *et al.*, 2009; Schall and van Hecke, 2010). As reported in Divoux *et al.* (2013), it can be argued that any experimental determination of the flow curve $\sigma(\dot{\gamma})$ is effectively transient since it is obtained by sweeping up or down the imposed shear rate $\dot{\gamma}(t)$ over a finite temporal window. Hence, the transient flow curve coincides with the steady-state constitutive relation only if the sweep rate is low enough compared to any intrinsic timescale of the fluid. Otherwise, *rheological hysteresis* is encountered. We define in Eq. (A1.1) an appropriate dimensionless parameter, \mathcal{H} , that enables a quantitative assessment of the extent of hysteresis in a given aging material,

$$\mathcal{H} = \int_{\dot{\gamma}_{\min}}^{\dot{\gamma}_{\max}} (\sigma^+ - \sigma^-) d\dot{\gamma} / \int_{\dot{\gamma}_{\min}}^{\dot{\gamma}_{\max}} \sigma^- d\dot{\gamma}. \tag{A1.1}$$

This parameter is computed as a ratio between the integral of the difference of the upper and lower measured flow curves (i.e., the enclosed area shown in Fig. 14) and the integral under the lower one (i.e., the area below the lowermost flow curve). For our initial experiments performed on Gillette foam, rheological hysteresis was repeatedly detected (Fig. 14, red curve) with a degree of hysteresis

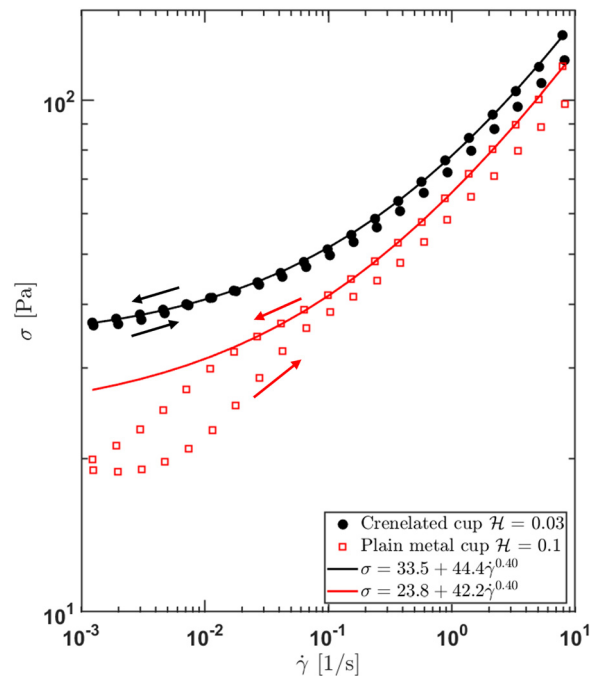


FIG. 14. Suppression of wall slip in a Gillette foam by the use of a crenelated cup with a 4-arm vane at $T = 25^\circ\text{C}$.

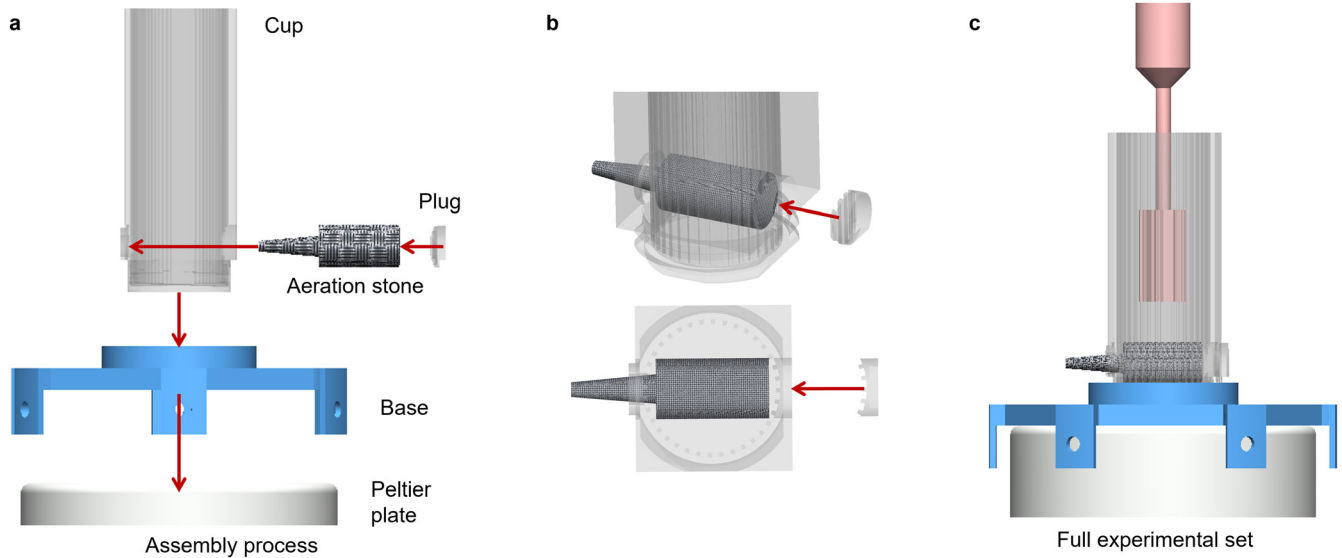


FIG. 15. Geometry set for testing transient rheology of coarsening foam *in situ*. (a) After printing, the aeration stone can be inserted in a large hole in the side of the cup. A plug with appropriate curvature and crenelations is glued in place after assembly, sealing the cup. Tubing can be attached to the opposite, extruded side of the aeration stone. When running experiments, the cup may be screwed down reversibly into the base, which is attached by double-sided tape to the Peltier plate in a position centered with the vane above. (b) A close-up shows the process of adding the plug to seal the cup after inserting the aeration stone. (c) The fully assembled set is shown together with an inserted 12-arm vane.

given by $\mathcal{H} \approx 0.1$, indicating non-negligible hysteresis. Direct observation of the material deformation during shearing experiments showed that this hysteretic behavior arises due to sample slip on the walls of the fixture.

To minimize this wall slip, a crenelated texture was added to the inner surface of the 3D-printed cup containing the foam. After this modification to the cup, the apparent hysteresis \mathcal{H} is reduced by more than a factor of three to $\mathcal{H} = 0.03$ (Fig. 14, black). Without this texture-driven reduction in the degree of wall slip, the determination of yield stress in these weak foams is substantially corrupted.

2. Bespoke rheometer tooling to measure foaming *in situ*

The printed items and assembly process are shown in Fig. 15. This includes printed items with the insertion of an aeration stone, and final sealing of the lower cavity using a printed plug and epoxy.

3. Mutation time and mutation number of foams

As stated in the text, to characterize the timescale of material evolution resulted fundamental to determine both the mutation time [$\lambda_{Mu}(t)$ Eq. (A3.1)] and the mutation number [$N_{Mu}(t)$ Eq. (A3.2)], as defined by Mours and Winter (1994),

$$\lambda_{Mu} = \left[\frac{1}{g} \frac{\partial g}{\partial t} \right]^{-1}, \quad (\text{A3.1})$$

$$N_{Mu} = \frac{\Delta t}{\lambda_{Mu}}. \quad (\text{A3.2})$$

Specifically, the former quantity provides the characteristic time constant for the change in the material properties, whereas the latter

provides an estimate of the change in material properties expected during an experiment.

To compute the evolution in both the mutation time and mutation number of the two foams, we fitted the measured values of both the elastic modulus $G'(t)$ and the loss modulus $G''(t)$ in time.

For the Gillette foam two fitting functions were chosen to better capture the evolution of the elastic modulus. A first exponential function from $t = 0$ s to $t = 10^3$ s according to Eq. (A3.3), and a second power law function from $t = 10^3$ s to $t = 10^5$ s (the end of the experiment) according to Eq. (A3.4):

$$G'_{fit1} = a_1 \exp(b_1 t) + c_1 \exp(d_1 t), \quad (\text{A3.3})$$

$$G'_{fit2} = A_1 t^{B_1} + C_1. \quad (\text{A3.4})$$

Similarly, the time-evolving loss modulus was fitted at short time by an exponential function, whereas at long times by polynomial function, Eqs. (A3.5) and (A3.6), respectively,

$$G''_{fit1} = a_2 \exp(b_2 t) + c_2 \exp(d_2 t), \quad (\text{A3.5})$$

$$G''_{fit2} = A_2 t^2 + B_2 t + C_2. \quad (\text{A3.6})$$

For the Chimec foam a single fitting function was selected for the elastic modulus [Eq. (A3.7)] and loss modulus [Eq. (A3.8)] evolutions, respectively,

$$G' = a_3 \exp(b_3 t) + c_3 \exp(d_3 t), \quad (\text{A3.7})$$

$$G'' = a_4 \exp(b_4 t) + c_4 \exp(d_4 t). \quad (\text{A3.8})$$

For small N_{Mu} , the rate of material mutation is small enough to be negligible in the analysis of an experiment, as we can confirm from consideration of Figs. 16(a)–16(d).

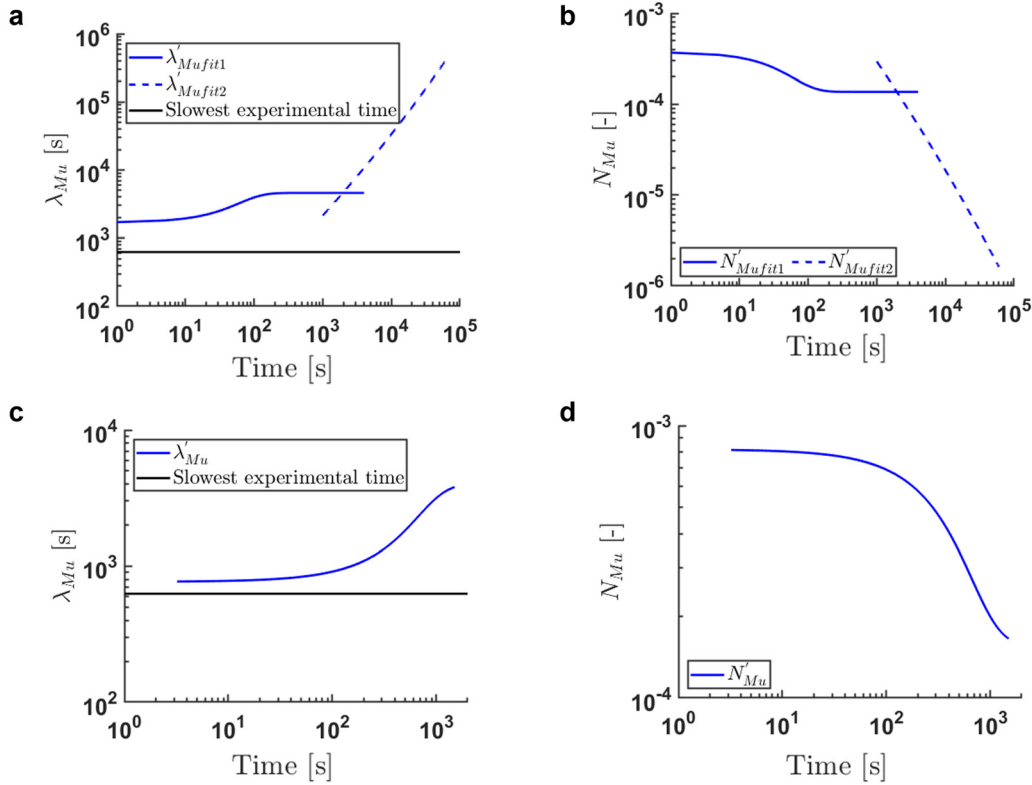


FIG. 16. (a) and (b) Evolution of the mutation time and mutation number for Gillette foam. (c) and (d) Mutation time and mutation number for Chimec foam.

4. Foam bubbles video procedure

Pictures were taken every 100 s, and subsequently concatenated into a single video, which can be used to see how the bubbles evolve in time. The video is available if required by the reader.

5. Creep tests on foams

To understand the aging of the foam under conditions of a constant imposed shear stress, creep tests were performed as reported in Fig. 17. Specifically, after a large elapsed time the Sauter mean radius $R_{32}(t)$ becomes large and the corresponding yield stress becomes so small that the foam starts collapsing under its own weight. The hydrostatic stress computed at the bottom of the cup can be compared to the yield stress of the foam to understand the critical value below which foam collapses. The maximum stress at the base can be determined using the following equation:

$$\sigma_{max} = \rho(1 - \phi)g(L + 2R_v). \tag{A5.1}$$

For the foam under analysis this expression gives $\sigma_{max} = 4.5$ Pa, which aligns with the results obtained through the creep tests. Referring to Fig. 17 in which the shear creep compliance $J(t) = \gamma(t)/\sigma_0$ is reported over time, we can identify three different regions:

- For $\sigma < \sigma_y \approx 4.5$ Pa the material does not yield and responds elastically,

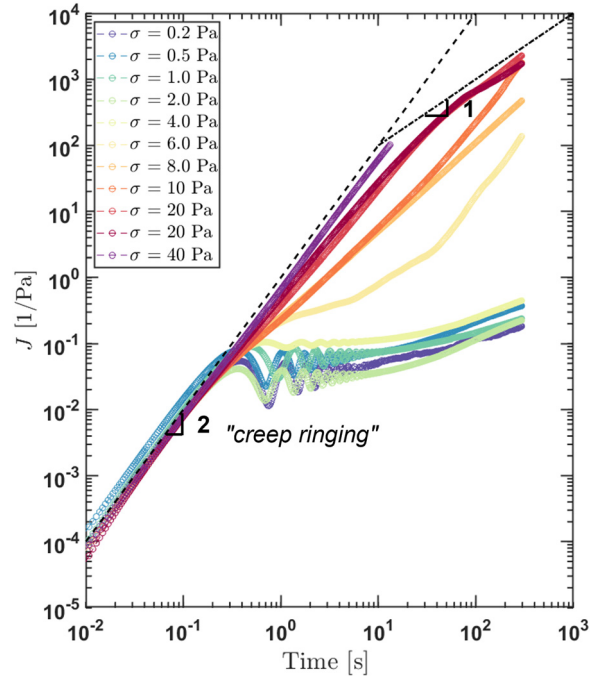


FIG. 17. Creep tests on Chimec foam at foam quality $\phi = 0.97$, with 12-arm vane in a 3D printed cup, $T = 25^\circ\text{C}$, and applied shear stresses ranging from $\sigma = 0.2$ to 40 Pa.

- For $\sigma > \sigma_y$, after yielding the material starts to flow,
- At $\sigma = 6$ Pa a delayed yielding phenomenon (Coussot *et al.*, 2006) is detected, likely due to foam degradation over time.

A more detailed consideration of Fig. 17 shows that at short times and at high stresses, the material shows a +2 power law index (i.e., $J \sim t^2$), linked to the fact that the moment of inertia of the instrument plays a major role in the reported compliance $J(t)$ at short times. Whereas, at long times and small stresses after steady plastic flow is established, a +1 power law index is observed in the evolving compliance. The reader may refer to Ewoldt and McKinley (2007) and Caton and Baravian (2008) for more details on the subject of creep ringing and inertioclastic responses.

6. Master curve for all foam quality tests

In the main text, the master curve for a foam quality of $\phi = 0.97$ is reported in Fig. 6(d). The time-evolving rheological data shown in Fig. 10 for other foam qualities also show self-similar aging dynamics. For completeness, we also show here (Fig. 18) the master curves that result from using the scaling expression for b_t given by Eq. (14) with the data reported in Table III.

7. Elastic modulus and viscous modulus shifting

The elastic modulus in a foam is also known to be proportional to the Laplace pressure (Dollet and Raufaste, 2014), and so the

same shifting paradigm can be applied to data shown previously in Fig. 5(a) from small amplitude oscillatory shear (SAOS) data [see also Fig. 13(b) in the main text]. We shift the measured SAOS data for both foams onto master curves using the independently determined evolution in the Sauter mean radius as shown in Fig. 19(a) for the Gillette foam and Fig. 19(b) for the Chimec foam. For both foams there is some divergence from a clear master curve in the loss modulus G'' at early times, which may be due to secondary drainage effects in young foams that are not captured in our equation model. Otherwise, the shift factors obtained from the measured evolution in the mean radius are in good agreement with the evolution in G' and of G'' , strongly suggesting that the evolution in linear viscoelastic properties with time is due primarily to the evolution in the mean bubble radius. The upturn in G'' in Fig. 19(a) at higher frequencies can be attributed to the increasing role of viscous dissipation as the foam ages, noted by a power law dependence of 1/2 in that region (Cohen-Addad *et al.*, 1998; Gopal and Durian, 2003). The obtained results for the Chimec foam align well with the ones reported in the open literature performed on the Gillette foam, even though the original data for predicting the radius evolution of the Gillette foam is derived from 30-year-old light scattering data (Durian *et al.*, 1991) as the small foam bubble size made imaging by light microscopy unfeasible; even so, it can be used to describe the time-dependent rheological evolution with some accuracy.

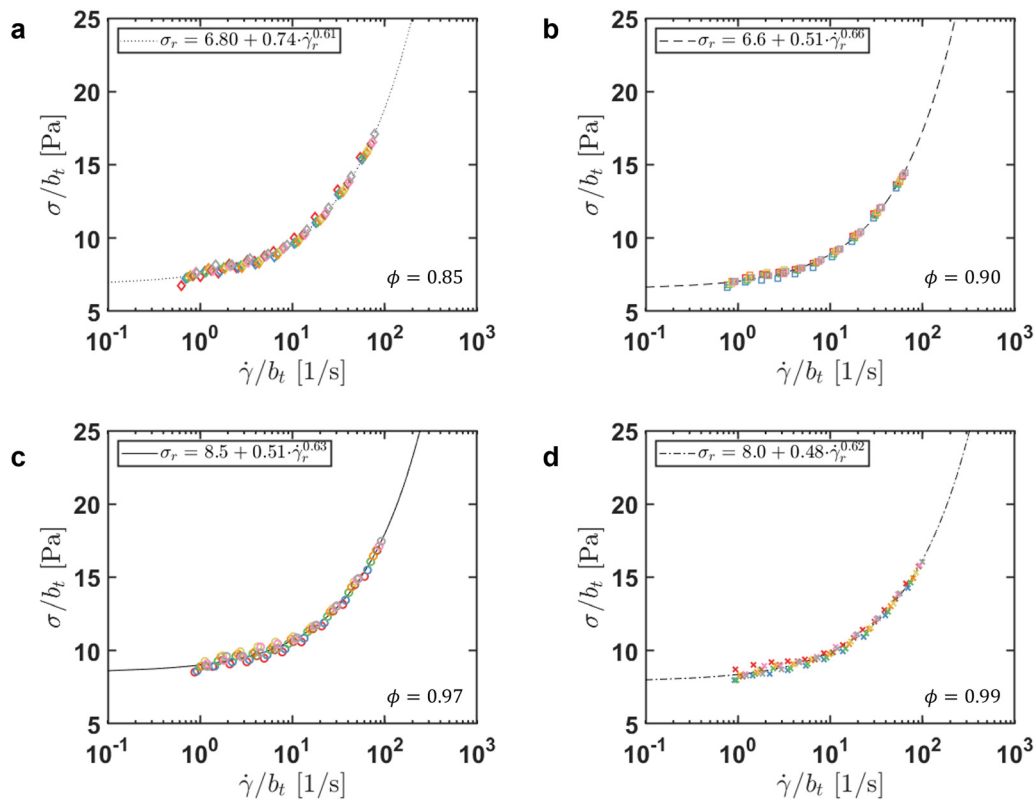


FIG. 18. Master curves constructed from the shifted torque and shifted rotational velocity using $t = 0$ as the reference age for the shift factor b_t for Chimec foams with (a) $\phi = 0.85$, (b) $\phi = 0.90$, (c) $\phi = 0.97$, and (d) $\phi = 0.99$.

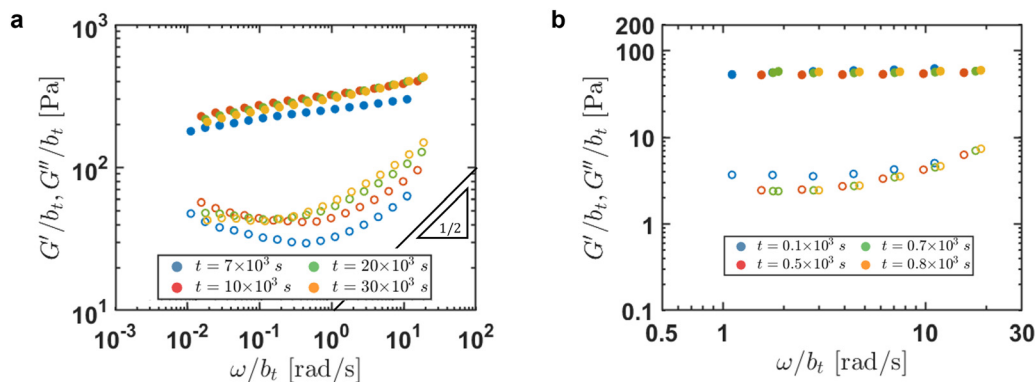


FIG. 19. Linear viscoelastic aging, showing the shifted values of the elastic modulus G' (filled symbols) and loss modulus G'' (hollow symbols) as function of shifted angular velocity, for (a) Gillette foam and (b) Chimec foam.

REFERENCES

- Atkinson, C., and Sherwood, J. D., "The torque on a rotating n -bladed vane in a Newtonian fluid or linear elastic medium," *Proc. R. Soc. London, Ser. A* **438**(1902), 183–196 (1992).
- Barik, T. K., and Roy, A., "Statistical distribution of bubble size in wet foam," *Chem. Eng. Sci.* **64**(9), 2039–2043 (2009).
- Bogdanovic, M., Gajbhiye, R. N., and Kam, S. I., "Experimental study of foam flow in horizontal pipes: Two flow regimes and its implications," *Colloids Surf., A* **344**, 56–71 (2009).
- Briceno, M. I., and Joseph, D. D., "Self-lubricated transport of aqueous foams in horizontal conduits," *Int. J. Multiphase Flow* **29**(12), 1817–1831 (2003).
- Calvert, J. R., and Nezhati, K., "A rheological model for a liquid-gas foam," *Int. J. Heat Fluid Flow* **7**(3), 164–168 (1986).
- Cantat, I., Cohen-Addad, S., Elias, F., Graner, F., Høhler, R., Pitois, O., Rouyer, F., and Saint-Jalmes, A., *Foams Structure and Dynamics* (Oxford University Press, 2013).
- Carraretto, I. M., Pari, D., Fasani, D., Lucchini, A., Guilizzoni, M. G., and Colombo, L. P. M., "Holdup measurements of aqueous foam flows and flow regime characterization through image processing," *SPE Prod. Oper.* **36**, 976 (2021).
- Caton, F., and Baravian, C., "Plastic behavior of some yield stress fluids: from creep to long-time yield," *Rheol. Acta* **47**(5–6), 601–607 (2008).
- Chaparian, E., Owens, C. E., and McKinley, G. H., "Computational rheometry of yielding and viscoplastic flow in vane-and-cup rheometer fixtures," *J. Non-Newtonian Fluid Mech.* **307**, 104857 (2022).
- Cohen-Addad, S., Hoballah, H., and Höhler, R., "Viscoelastic response of a coarsening foam," *Phys. Rev. E* **57**(6), 6897–6901 (1998).
- Cohen-Addad, S., and Höhler, R., "Rheology of foams and highly concentrated emulsions," *Curr. Opin. Colloid Interface Sci.* **19**(6), 536–548 (2014).
- Collias, D. I., and Baird, D. G., "Tensile toughness of microcellular foams of polystyrene, styrene-acrylonitrile copolymer, and polycarbonate, and the effect of dissolved gas on the tensile toughness of the same polymer matrices and microcellular foams," *Polym. Eng. Sci.* **35**(14), 1167–1177 (1995).
- Collias, D. I., Baird, D. G., and Borggreve, R. J. M., "Impact toughening of polycarbonate by microcellular foaming," *Polymer* **35**(18), 3978–3983 (1994).
- Colombo, L. P. M., Carraretto, I. M., Di Lullo, A. G., Passucci, C., and Allegrucci, A., "Experimental study of aqueous foam generation and transport in a horizontal pipe for deliquification purposes," *Exp. Therm. Fluid Sci.* **98**, 369–380 (2018).
- Coussot, P., Tabuteau, H., Chateau, X., Tocquer, L., and Ovarlez, G., "Aging and solid or liquid behavior in pastes," *J. Rheol.* **50**(6), 975–994 (2006).
- Dall'Acqua, D., Benucci, M., Corvaro, F., Leporini, M., Cocci Grifoni, R., Del Monaco, A., Lullo, A. D., Passucci, C., and Marchetti, B., "Experimental results of pipeline dewatering through surfactant injection," *J. Pet. Sci. Eng.* **159**, 542–552 (2017).
- Dinkgreve, M., Paredes, J., Denn, M. M., and Bonn, D., "On different ways of measuring 'the' yield stress," *J. Non-Newtonian Fluid Mech.* **238**, 233–241 (2016).
- Divoux, T., Grenard, V., and Manneville, S., "Rheological hysteresis in soft glassy materials," *Phys. Rev. Lett.* **110**(1), 018304 (2013).
- Dollet, B., and Raufaste, C., "Rheology of aqueous foams," *C. R. Phys.* **15**(8–9), 731–747 (2014).
- Durian, D. J., Weitz, D. A., and Pine, D. J., "Scaling behavior in shaving cream," *Phys. Rev. A* **44**, R7902 (1991).
- Ellis, A. L., and Lazidis, A., in *Foams for Food Applications BT—Polymers for Food Applications*, edited by Tomy J. Gutiérrez (Springer International Publishing, Cham, 2018), pp. 271–327.
- Ewoldt, R. H., and McKinley, G. H., "Creep ringing in rheometry or how to deal with oft-discarded data in step stress tests!," *Rheol. Bull.* **76**, 4–6 (2007).
- Gajbhiye, R. N., and Kam, S. I., "Characterization of foam flow in horizontal pipes by using two-flow-regime concept," *Chem. Eng. Sci.* **66**(8), 1536–1549 (2011).
- Gopal, A. D., and Durian, D. J., "Relaxing in foam," *Phys. Rev. Lett.* **91**(18), 188303 (2003).
- Gunton, J. D., San Miguel, M., and Sahni, P. S., in *Phase Transitions and Critical Phenomena*, edited by C. Domb, and J. L. Lebowitz (Academic London, 1983).
- Herzhaft, B., Kakadjian, S., and Moan, M., "Measurement and modeling of the flow behavior of aqueous foams using a recirculating pipe rheometer," *Colloids Surf., A* **263**(1–3), 153–164 (2005).
- Hilgenfeldt, S., Koehler, S. A., and Stone, H. A., "Dynamics of coarsening foams: Accelerated and self-limiting drainage," *Phys. Rev. Lett.* **86**(20), 4704–4707 (2001).
- Höhler, R., and Cohen-Addad, S., "Rheology of liquid foam," *J. Phys.: Condens. Matter* **17**(41), R1041 (2005).
- Khan, S. A., and Armstrong, R. C., "Rheology of foams: I. Theory for dry foams," *J. Non-Newtonian Fluid Mech.* **22**, 1–22 (1986).
- Khan, S. A., and Armstrong, R. C., "Rheology of foams: II. Effects of polydispersity and liquid viscosity for foams having gas fraction approaching unity," *J. Non-Newtonian Fluid Mech.* **25**, 61–92 (1987).
- Lambert, G. M., and Baird, D. G., "Evaluating rigid and semiflexible fiber orientation evolution models in simple flows," *J. Manuf. Sci. Eng., Trans. ASME* **139**(3), 031012 (2017).
- Mours, M., and Winter, H. H., "Time-resolved rheometry," *Rheol. Acta* **33**, 385–397 (1994).
- Nguyen, Q. D., and Boger, D. V., "Characterization of yield stress fluids with concentric cylinder viscometers," *Rheol. Acta* **26**(6), 508–515 (1987).
- Ovarlez, G., Cohen-Addad, S., Krishan, K., Goyon, J., and Coussot, P., "On the existence of a simple yield stress fluid behavior," *J. Non-Newtonian Fluid Mech.* **193**, 68–79 (2013).
- Ovarlez, G., Rodts, S., Chateau, X., and Coussot, P., "Phenomenology and physical origin of shear localization and shear banding in complex fluids," *Rheol. Acta* **48**(8), 831–844 (2009).

- Owens, C. E., Hart, A. J., and McKinley, G. H., "Improved rheometry of yield stress fluids using bespoke fractal 3D printed vanes," *J. Rheol.* **64**(3), 643–662 (2020).
- Parikh, D., Wu, Y., Peterson, C., Jarriel, S., Mooney, M., and Tilton, N., "The coupled dynamics of foam generation and pipe flow," *Int. J. Heat Fluid Flow* **79**, 108442 (2019).
- Pitois, O., and Rouyer, F., "Rheology of particulate rafts, films, and foams," *Curr. Opin. Colloid Interface Sci.* **43**, 125–137 (2019).
- Polyanin, A. D., Kutepov, A. M., Vyazmin, A. V., and Kazenin, D. A., "Foams: Structure and some properties," in *Hydrodynamics, Mass and Heat Transfer in Chemical Engineering* (CRC Press, 2002).
- Princen, H. M., "Rheology of foams and highly concentrated emulsions. I. Elastic properties and yield stress of a cylindrical model system," *J. Colloid Interface Sci.* **91**(1), 160–165 (1983).
- Princen, H. M., "Rheology of foams and highly concentrated emulsions. II. Experimental study of the yield stress and wall effects for concentrated oil-in-water emulsions," *J. Colloid Interface Sci.* **105**(1), 150–171 (1985).
- Princen, H. M., "A novel design to eliminate end effects in a concentric cylinder viscometer," *J. Rheol.* **30**(2), 271–283 (1986).
- Princen, H. M., and Kiss, A. D., "Rheology of foams and highly concentrated emulsions. III. Static shear modulus," *J. Colloid Interface Sci.* **112**(2), 427–437 (1986).
- Princen, H. M., and Kiss, A. D., "Rheology of foams and highly concentrated emulsions. IV. An experimental study of the shear viscosity and yield stress of concentrated emulsions," *J. Colloid Interface Sci.* **128**(1), 176–187 (1989).
- Qian, C., and Baird, D. G., "The transient shear rheology of a thermotropic liquid crystalline polymer in the super-cooled state," *Polymer* **102**, 63–72 (2016).
- Saint-Jalmes, A., "Physical chemistry in foam drainage and coarsening," *Soft Matter* **2**(10), 836–849 (2006).
- Saint-Jalmes, A., Durian, D. J., and Weitz, D. A., "Foams," in *Encyclopedia of Chemical Technology*, edited by Kirk-Othmer (John Wiley & Sons, Inc., 2012).
- Saint-Jalmes, A., and Langevin, D., "Time evolution of aqueous foams: Drainage and coarsening," *J. Phys.: Condens. Matter* **14**(40), 9397–9412 (2002).
- Schall, P., and van Hecke, M., "Shear bands in matter with granularity," *Annu. Rev. Fluid Mech.* **42**(1), 67–88 (2010).
- Schramm, L. L., *Emulsions, Foams, and Suspensions: Fundamentals and Applications* (Wiley-VCH, 2006).
- Stevenson, P., *Foam Engineering: Fundamentals and Applications* (John Wiley and Sons, 2012).
- Tiratsoo, J., in *Pipeline Pigging and Integrity Technology*, edited by J. Tiratsoo (Clarion Technical Publishers, 2003).
- Weaire, D., "The rheology of foam," *Curr. Opin. Colloid Interface Sci.* **13**(3), 171–176 (2008).